Award Number: W81XWH-16-1-0004

TITLE: Lymph Node Metastases Optical Molecular Diagnostic and Radiation Therapy

PRINCIPAL INVESTIGATOR: Brian Pogue

CONTRACTING ORGANIZATION: Trustees of Dartmouth College
                                        Hanover, NH 03755

REPORT DATE: March 2017

TYPE OF REPORT: Annual

PREPARED FOR: U.S. Army Medical Research and Materiel Command
                    Fort Detrick, Maryland 21702-5012

DISTRIBUTION STATEMENT: Approved for Public Release;
                                    Distribution Unlimited

The views, opinions and/or findings contained in this report are those of the author(s) and should not be construed as an official Department of the Army position, policy or decision unless so designated by other documentation.

REPORT DOCUMENTATION PAGE

1. REPORT DATE	2. REPORT TYPE	3. DATES COVERED
March 2017	Annual	1 Mar 2016 - 28 Feb 2017

4. TITLE AND SUBTITLE	5a. CONTRACT NUMBER
Lymph Node Metastases Optical Molecular Diagnostic and Radiation Therapy	5b. GRANT NUMBER W81XWH-16-1-0004
	5c. PROGRAM ELEMENT NUMBER

6. AUTHOR(S)	5d. PROJECT NUMBER
Brian W Pogue	5e. TASK NUMBER
	5f. WORK UNIT NUMBER
E-Mail: brian.w.pogue@dartmouth.edu	

7. PERFORMING ORGANIZATION NAME(S) AND ADDRESS(ES)	8. PERFORMING ORGANIZATION REPORT NUMBER
Trustees of Dartmouth College Thayer School of Engineering 14 Engineering Drive Hanover NH 03755	

9. SPONSORING / MONITORING AGENCY NAME(S) AND ADDRESS(ES)	10. SPONSOR/MONITOR'S ACRONYM(S)
U.S. Army Medical Research and Materiel Command Fort Detrick, Maryland 21702-5012	
	11. SPONSOR/MONITOR'S REPORT NUMBER(S)

12. DISTRIBUTION / AVAILABILITY STATEMENT

Approved for Public Release; Distribution Unlimited

13. SUPPLEMENTARY NOTES

14. ABSTRACT

Breast cancer metastases detection, imaging and management is limited by a key technical problem fundamental to the nature of imaging, which is that micro metastases cannot be visualized at a relevant stage, largely because most imaging is based upon structures and not molecular functions. The one tool commonly used for metastases imaging is nuclear medicine. Positron emission tomography, PET, is used for whole body imaging, of metastases, or Gamma probe imaging is used for sentinel lymph node detection. PET is extremely successful in clinical staging based upon detection of involvement in lymph nodes and secondary organs, but there are no tools to effectively sense early metastases. Gamma imaging of sentinel nodes is not a disease diagnostic, but rather just used to find the node and remove it for pathological inspection. As a result, we are in a situation where surgical node dissection procedures are the standard for detection and removal of metastases, but axillary node dissection has high morbidity and is only needed in about 25% of cases that it is done it. Surgical dissection is the result of the fact that there is no molecular imaging tool today which can routinely sense the presence of cancer cells in lymph nodes or organs at the micrometastases stage. The needed probe sensitivity would be in the uM to nM range with sub mm spatial resolution throughout the body. This lack of high spatial resolution molecular imaging is a key factor inhibiting breast metastases research and treatment.

15. SUBJECT TERMS

Radiotherapy, Cherenkov, imaging, tomography, metastases

16. SECURITY CLASSIFICATION OF: U			17. LIMITATION OF ABSTRACT	18. NUMBER OF PAGES	19a. NAME OF RESPONSIBLE PERSON USAMRMC
a. REPORT Unclassified	b. ABSTRACT Unclassified	c. THIS PAGE Unclassified	Unclassified	32	19b. TELEPHONE NUMBER *(include area code)*

Table of Contents

        Addressing overlap with recently funded NIH grant R01EB024498-01

        Published paper "Cherenkov Excited Luminescence Scanned Imaging
        provides the highest resolution & molecular sensitivity for pre-clinical
        whole body imaging"

1. INTRODUCTION:

Breast cancer metastases detection, imaging and management is limited by a key technical problem fundamental to the nature of imaging, which is that micro metastases cannot be visualized at a relevant stage., largely because most imaging is based upon structures and not molecular functions. But there are no tools to effectively sense early metastases, and this lack of high spatial resolution molecular imaging is a key factor inhibiting breast metastases research and treatment. In this proposal, we develop a completely unique hybrid modality which will have high resolution capability through several centimeters of tissue, and all the molecular specificity of standard optical luminescence tracers, with sensitivity down to the sub uM level and spatial resolution below 1mm. The new approach uses high energy x-rays from a linear accelerator, LINAC, used in radiation therapy, allowing metabolic imaging and treatment in the same setting. The LINAC radiation induces Cerenkov light in the tissue, and this light can excites luminescence for molecular imaging. This Cerenkov-excited luminescence scanned imaging approach is referred to as CELSI throughout this work. We proposed to develop the two unique parts to this tool, and test it as combined with multi-probe imaging, to quantify the molecular microenvironment of cancer tumors in vivo.

The individual aims in this overall goal are (1) to optimize the setup and design of a dedicated system to sense signals. (2) To design and build a dedicated system suitable for imaging signals from in small animals on the standard radiation therapy tools. (3) To evaluate the limits on structural, metabolic and immunologic probes for molecular imaging, and (4) to complete studies on metastatic breast cancer with MeV photon imaging and treatment.

CELSI has been demonstrated at the initial in vivo feasibility stage in a lymph node imaging study (Zhang et al Opt. Lett 2015), and should be evaluated as a fundamentally new molecular imaging modality. We anticipate the as the ability to sense molecular concentrations at low radiation dose gets established that human use possibilities will be discovered, either as a therapy/diagnosis tool in Radiation Oncology or purely as a low dose diagnostic.

2. KEYWORDS:

Radiotherapy, Cerenkov, Cherenkov, imaging, tomography, sentinel, lymph node, metastases, detection, staging, therapy.

3. ACCOMPLISHMENTS: *The PI is reminded that the recipient organization is required to obtain prior written approval from the awarding agency Grants Officer whenever there are significant changes in the project or its direction.*

- **What were the major goals of the project?**

Tasks	Timeline	Site 1 (PI Pogue)	Site 2 (PI Jarvis & Gladstone)
Major Task 1: Development of a high-resolution molecular imaging system	Months	Engineering	Radiation Oncology
Subtask 1: Evaluate components for optimal CELSI system • oversee system development, detector choice & evaluation • Monte Carlo modeling of detection & geometry	1-6 3-6	Bruza & Pogue	
Subtask 2: Determine the limits to detection for CELSI • Dr Pogue's lab: testing limits, SNR, CBR, for relevant targets • Dr. Gladstone's lab: evaluate the performance in linac use, testing dose requirements. • Dr. Jarvis's lab: estimate limits for lymph node detection in animals & humans	7-10 11-12		Dr Gladstone & Gollub Gunn & Jarvis
Milestones: *quantify possible tradeoffs on:depth, ii) radiation dose, and iii) probe concentration* *identify realistic limits for radiation dose & probe concentration for lymph node imaging* *identify realistic limits for tumor imaging with intravascular & interstitial delivery* *Publication on limits and potential for CELSI imaging (Phys. Med. Biol.)*			
Major Task 2: Design and build a dedicated system for CELSI imaging in small animals, to allow imaging of molecular probes in a manner which has maximal spatial, temporal and contrast resolution.		Engineering	Radiation Oncology
Subtask 1: Completion of an optimized system for delivery to Radiation Oncology	13-18	LaRochelle & Pogue	

Subtask 2: Implementation in radiation oncology & initial animal testing.	19-21		LaRochelle, Gladstone & Gunn
Milestones: *Delivery of completed system capable of 200 micron resolution & imaging 2 cm deep into tissue* *Co-author manuscript on system and construction (Optics Letters)*			
Major Task 3: Evaluate the quantitative limits on structural, metabolic and immunologic probes for metastatic breast cancer molecular imaging with CELSI and establishing Standard Uptake Values (SUV).		Engineering	Radiation Oncology
Subtask 1: Evaluating molecular probes for use	22-24	Pogue	Gunn
Subtask 2: Establish SUV value in vivo	25-28	Pogue	Gunn & Jarvis
Milestones: *Demonstrated limits to detection for metabolic & immunologic probes.* *Publication on CELSI & SUV of different molecular probes (Science Translational Medicine)*			
Major Task 4: Complete metastatic breast cancer detection & treatment with MeV photon treatment		Engineering	Radiation Oncology
Subtask 1: complete metastatic & non-metastastic imaging studies in vivo	29-34	Pogue	Gunn & Jarvis
Subtask 2: complete radiation treatment study on involved nodes	34-36		Gunn & Jarvis
Milestone #4: demonstration of in vivo detection and limits to numbers of cells detectable in lymph nodes *Publication on in vivo detection & treatment using CELSI and radiation therapy (Int. J. Rad. Oncol. Biol. Phys.).*			

What was accomplished under these goals?

This year, we completed Major Task 1 as planned.

In **Subtask 1** of Major Task 1, Dr Pogue and his laboratory (Bruza, Gollub, LaRochelle) focused efforts on optimizing the experimental system geometry in terms of (i) assessment of fluorophores, (ii) optimization of spatial resolution, (iii) modeling of the raw data versus reconstructed data, so that we can optimally define the approach and characteristics of the CELSI system. Each of these are described here:

i.   **In fluorphore/phosphore development,** we completed a series of phantom studies to assess which agents would have th highest signal strength as well as biological compatibility. The imaging geometry is as shown below in figure 1(a) and photographed in (b). We assessed a range of 6 lead candidate agents, including our first agent, PtG4, and now this list includes two Iridium complexes, two cryptate complexes LuAg:CeMg and LuAu:CeMg, and two commercial oxygen sensors optimized for cell/tissue use, MM2 and MitoID. **Based upon signal intensity the LuAG:CeMg was the best, but in terms of oxygen sensitive signal, the Iridium complexes were superior.** Going forward we will focus on these the iridium complex, MM2 and PtG4 which will be incubated into cells next, and similar study completed.
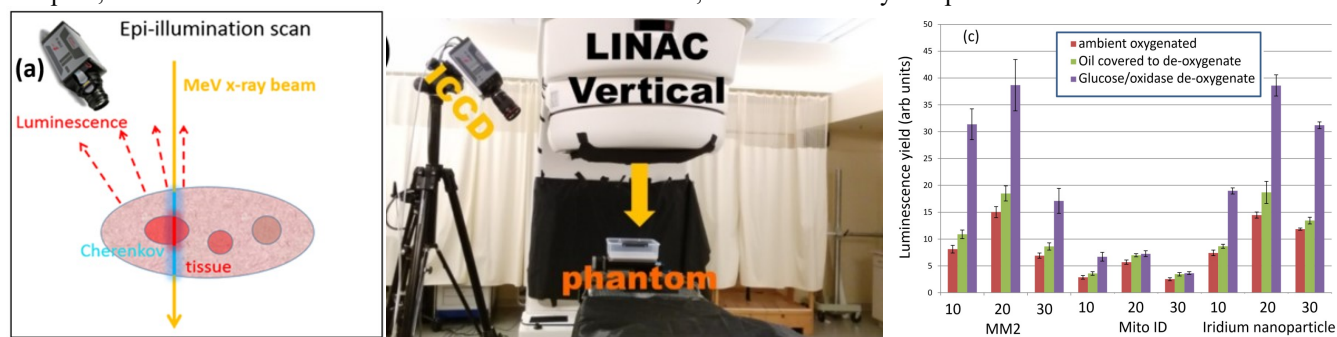

Figure 1. The set up with ICCD camera, gated to the LINAC radiation beam delivery is shown schematically in (a) with the photograph in (b). This set up was used to test phosphorescence of 3 biologically relevant phosphors that have sensitivity to oxygen, MM2, MitoID and an iridium complex nanoparticle. The data from these three were the best of all 6 compounds

4

tested, and the data shown for 3 concentrations (10, 20 and 30 nanoMolar), as shwn in (c). Deoxygenation of each was done to see the relative increase in luminescence from non-quenching by oxygen.

ii.   **In terms of defining the detected spatial resolution,** we have now completed an extensive series of resolution tests and reconstructions. Initially computer simulations of the geometry and target recovery were completed with two objects varied in distance, a classic resolution test, to discern when the two objects could not be resolved from each other. Thee simlulations (a) and the summary graph (b) are shown in figure 2 below. Next meausurements of single cylinders containing phosphorescent PtG4 were used from 1.0mm down to 0.1mm, to test the recovery of the profile width, as a single target test of spatial resolution. The geometry, cylinders and resulting summary graph are also shown below in Figure 2 (c)-(e). Both simulations and experiments indicate that the spatial resolution limit is near 0.1-0.2mm (ie. see blue line in figure 2(b), and the limit of FWHM observed in figure 2(d)). **This indicates positive potential for imaging a lymph node (size scale 2-3mm),since the spatial resolution is far better than this.**
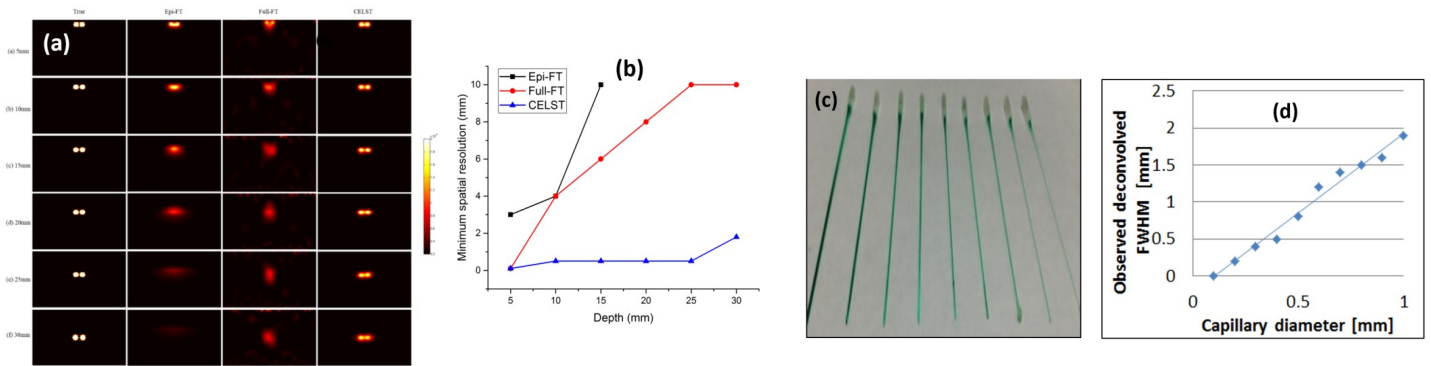

Figure 2 (a) Capillaries filled with PtG4 are shown (a) and were embedded into a tissue equivalent phantom, and a sheet beam scanned laterally to extract the FWHM for each sized tube (b). To establish the theoretical limits to spatial resolution, reconstructed results using the CELST for two inclusions with varied edge-to-edge distance in different depths are shown, (c). For each depth the minimum resolvable distance was estimated and plotted in (d), for both diffuse fluorescence tomography, epi-illumination fluorescence tomography and CESLI tomography.

iii.   **Computer modeling simulations of the raw data and reconstruction** indicated that recovery of objects within the tissue like media can be recovered down to 30mm deep, with a limiting step size of the collimators shaping the beam. This can be seen in figure 2(b) above. Additionally, we examined beam scan geometries and demonstrated how to use spatial deconvolution and depth dependent attenuation correction to linearize the recovered images. The paper by Bruza in Optics Letters utilized linear deconvolution and attenuation corrections (shown below in figure 3) and the study we are just about to submit showed how to use non-linear diffuse optical tomography reconstruction to recover similar images (shown in figure 4). We will continue in the next year to test both methods with experimentally measured data as planned in the next tasks.
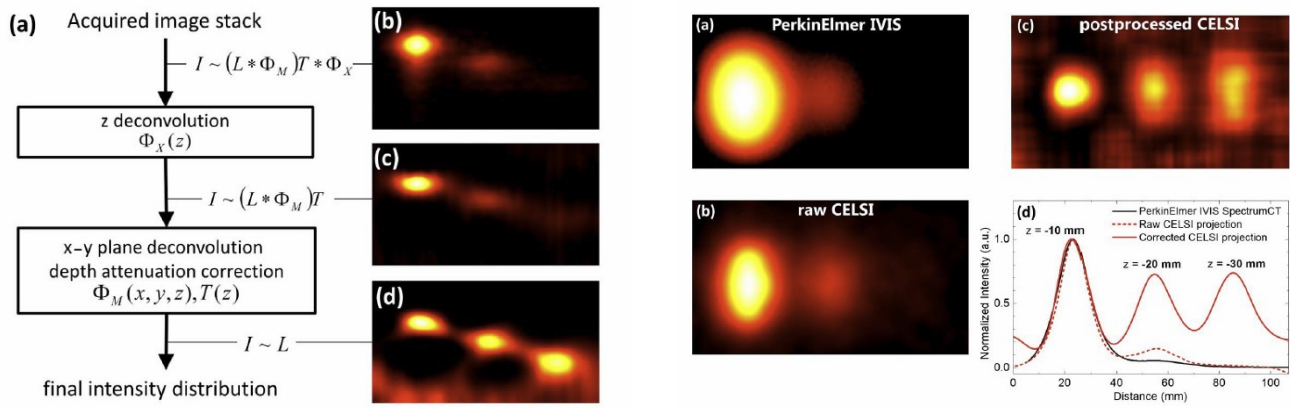
Figure 3. The process of image recovery is shown from Bruza et al, optics Letters 2016, where the acquired image stack from a tissue phantom having 3 luminescent rods in it, shown as a profile depth scan here in (b), with a depth of 3cm and lateral extent of 8cm. The three rolds are located 10mm, 20mm and 30mm down into the medium. The z-axis deconvolution is applied to recovery (c) and then depth dependent attenuation correction is applied to recover (d). On the right, comparisons of imaging the same phantom are done with the commercial PerkinElmer IVIS system and displayed from the top view, as well as the raw CELSI image data and the postprocessed image. The recovery with these linear processing methods demonstrates our ability to image luminescence down through 3 cm of tissue equivalent material.
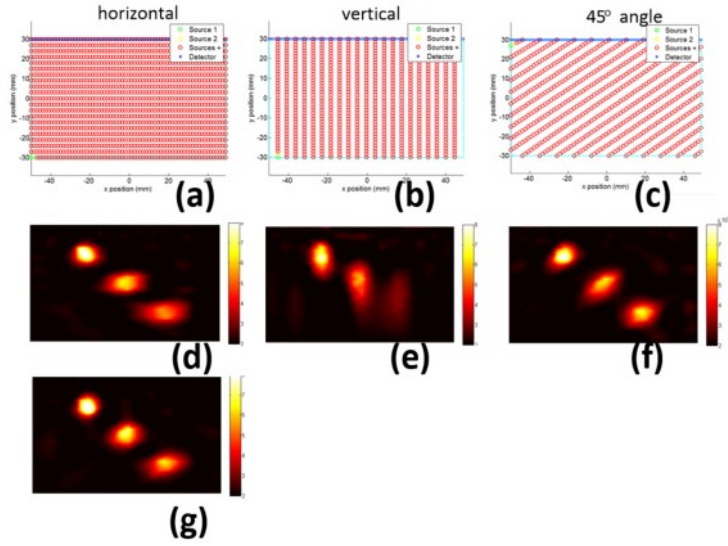

Figure 4. Computer simulations with the iterative reconstruction code NIRFAST were carried out on the same geometry as was used in Figure 3. The recovery of images was very good for three different scan geometries, as illustrated in (a) (b) and (c). The corresponding images are shown in (d), (e) and (f), and the combination of all 3 scan sequences into a single image recovered the best image (g).

These simulations confirmed for the first time that either the linear method or the non-linear reconstruction method, could allow reovery of CELSI images down to 30mm in tissue like media. **In summary, we believe that we have completed subtask 1 in Dr Pogue's laboratory.**

In **Subtask 2** of Major Task 1, Dr Jarvis's laboratory (Gladstone, Gunn, with Bruza & Gollub supporting) focused their efforts on (i) testing limits, SNR, CBR, for relevant targets, (ii) evaluation of the performance in linac use, testing dose requirements, and (iii) estimating limits for lymph node detection in animals & humans. Each of these is described below:

i.   The dominant factors affecting image recovery were explored systematically by varying one parameter at a time. The contrast to background ratio was used as a metric of success, assessing how this varied with radiation dose delivered, concentration of PtG4 and depth of the object into the medium. CELSI of PtG4 in a 1mm diameter capillary was assessed with different

concentrations, depths (distance from capillary to phantom surface) and radiation doses. First using a fixed depth of 5mm, the concentrations range was varied logarithmically from 500 mM down to 0.78 uM measuring contrast to background ratio for a 1 second acquisition time. The results are shown in Fig 5(a), being monotonic in shape and reducing to a contrast to background ratio of 1 at about 2 uM. Next the CBR was tracked for a fixed concentration of 50 uM, varying the depth down to 20mm into the phantom. This was monotonic with depth and appears to decrease near CBR=1 well beyond the 20mm depth. Finally, the variation with radiation pulses added together was studied at a target depth of 5mm and fixed concentration of 50 uM, showing monotonic dependence on dose, and decreasing to CBR of 1 at 2 radiation pulses, roughly equivalent to 0.06 cGy dose.

Figure 5. Contrast to Background Ratio (CBR) measurements from PtG4 contained within a 1mm capillary with (a) different concentrations in the physiologically relevant range, (b) varying depth between the capillary wall to the surface of the phantom being imaged, and (c) varying radiation dose between 1 and 500 radiation pulses. The concept of how each of these three factors has a reciprocal effect upon the signal to noise is illustrated in (d).

This parameter space is now well defined, and is summarized in our paper about to be submitted, allowing to assess for a lymph node of a certain size and depth, what concentration agent would be required, and this is in the range of 1-10 uM.

ii.   In terms of linac performance, we created a software tool to allow creation of multi-leaf collimator changes, for research use. **This tool was then implemented as a routine way to shape the sweeping of the beam for CELSI imaging.**

iii.   We completed a pilot study of imaging a lymph node sized object in mice tissue and in a mouse phantom, as seen below in Figure 6. The mouse phantom data was most useful to determine if the signal was detectable, and **we found that at the concentrations prescribed above (1-10 uM) we were able to accurately image a lymph node sized object in both the mouse phantom as well as embedded into the mouse tissue.**
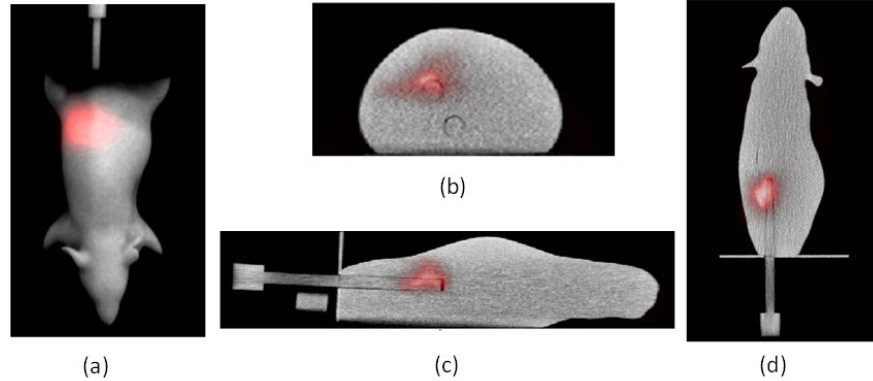

Figure 6. The phantom experiment. (a) The luminescent images overlaid on the top surface of the CT images; (b) are the reconstructed images shown with 3 orthogonal views, coronal, sagittal and transverse.

In summary, subtask 2 was completed as planned by the Jarvis Laboratory.

▪   **What opportunities for training and professional development has the project provided?**

Sarah Gollub (post doc) & Ethan LaRochelle (PhD student) both obtained knowledge and mentoring about how to run the linear accelerators, how to acquire data with the cameras, and how to process the data. Ethan LaRochelle is attending the Biophotonics '17 summer school in Sweden, June 2017.

▪   **How were the results disseminated to communities of interest?**

One Peer-reviewed Publication was published this past year, and we have one other one in preparation, as are listed below. We have also produced 4 conference abstracts, as are listed below.

▪   **What do you plan to do during the next reporting period to accomplish the goals?**

In this next year we plan to significantly advance our goals of finding the limits to lymph node size detection with different agents. We will be taking our chosen phosphors into cells and then into rodents to assess in vivo potential. We plan to test a new fast detector which has recently been introduced by Becker&Hickl which should allow superior temporal sampling and therefore improve our ability to use fluorophores with nanosecond lifetimes.

We have staffing changes which will significantly amplify our ability to get the work done faster and will allow a wider range of activities, by having smaller percentages of a larger number of people involved, adding a wider expertise base and better collaborative capabilities.

4.   **IMPACT:** *Describe distinctive contributions, major accomplishments, innovations, successes, or any change in practice or behavior that has come about as a result of the project relative to:*

▪   **What was the impact on the development of the principal discipline(s) of the project?**

We demonstrated for the first time that recovery of luminescent objects could be recovered from depths near 3cm in tissue simulating media. This was published in our paper Bruza et al, Opt. Lett, and showed that by Cherenkov excitation and data collection, combined with depth-dependent attenuation correction, that there is excellent recovery. This depth of accurate optical imaging has not been possible before.

In our paper being submitted to Nature BME, we demonstrate that the spatial resolution of CELSI is exceptionally high (near 200 microns) at 25-30mm into the medium, whereas when we compare that directly to diffuse fluorescence tomography or subsurface fluorescence, the spatial resolution drops as $r = 0.2D$, where D is the depth and r is the lateral spatial resolution. So at 25mm depth tomography has a resolution of 5mm, or 5000 microns. Thus in this 0 to 25 mm depth range, the spatial resolution can be improved by nearly 25x with CELSI imaging. The niche role that CELSI can play in molecular imaging is illustrated below in Figure 7, placing axes around the spatial resolution for whole body mouse imaging against the molecular sensitivity of the method. As can be seen, CELSI has the lowest sensitivity and lowest spatial resolution, placing it with potentially high impact for key molecular imaging studies of cell metabolites and immunological signaling. This also shows that CELSI has the spatial resolution to image lymph nodes. Anthropomorphic mouse phantoms and a mouse model of implanted cancer were also used in the paper to demonstrate the ability to image in mouse shaped heterogeneous media. Recovery of the spatial resolution was near 200 microns accuracy.

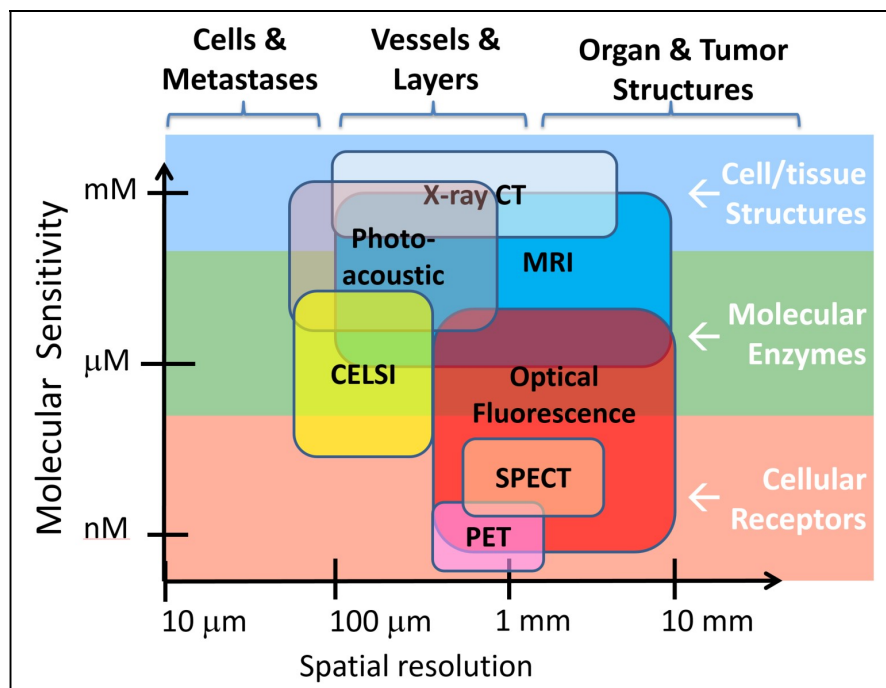**Figure 7** shows an illustration of the characteristics where Cherenkov excited sheet luminescence imaging (CELSI) can achieve is shown relative to other whole body imaging modalities. The need for high spatial resolution with low molecular sensitivity provides the ability detect and image cellular metabolic and immunologic activities in vivo.

▪   **What was the impact on other disciplines?**

Nothing to report

- **What was the impact on technology transfer?**

Nothing to report to date.

- **What was the impact on society beyond science and technology?**

The capabilities of CELSI will allow more useful detection of small objects inside tissue, such as lymph nodes involved with breast cancer. This could have wide ranging implications on how metastatic breast cancer is managed. It is hoped that this high-resolution imaging at the 0 – 3 cm depth range will provide the tool needed to interrogate lymph nodes and help surgeons make a decision about whether to resect them or not. If this works, it would reduce the number of patients with morbidity associated with lymphedema.

5. **CHANGES/PROBLEMS:**

- **Changes in approach and reasons for change**

  Nothing to report.

- **Actual or anticipated problems or delays and actions or plans to resolve them**

  Nothing to report.

- **Changes that had a significant impact on expenditures**

  We have had minor staffing changes, as is normal with a new project, having shifted responsibilities between one post doc (Petr Bruza) to anther (Sarah Gollub) and now recruited a new graduate student to the project (Ethan LaRochelle) and getting reconstruction guidance from a former laboratory member (Jinchao Zhang). But while organizing this has delayed some of the activities in year 1 a bit more than would have been desired, things are now set to advance the work much more quickly than planned for year 2. So we are extremely optimistic that we will have completed more than promised by the end of year 2.

- **Significant changes in use or care of human subjects, vertebrate animals, biohazards, and/or select agents**

  nothing to report

- **Significant changes in use or care of human subjects** – nothing to report.

- **Significant changes in use or care of vertebrate animals.** – nothing to report.

- **Significant changes in use of biohazards and/or select agents** – nothing to report.

6. **PRODUCTS:** *List any products resulting from the project during the reporting period. If there is nothing to report under a particular item, state "Nothing to Report."*

- **Publications, conference papers, and presentations**

- **Journal publications.**

Brůža P, Lin H, Vinogradov SA, Jarvis LA, Gladstone DJ, Pogue BW. "Light sheet luminescence imaging with Cherenkov excitation in thick scattering media." Opt Lett. 2016 Jul 1;41(13):2986-9. doi: 10.1364/OL.41.002986. – Federal support is acknowledged in this paper.

B. W. Pogue, J. Feng, H. Lin, P. Bruza, E. LaRochelle, R. Zhang, H. Dehghani, S. C. Davis, S. Vinogradov, D. J. Gladstone, L. A. Jarvis "Molecular Cherenkov Excited Luminescence Scanned Imaging In Vivo: highest resolution & sensitivity for pre-clinical whole

body imaging" (manuscript drafted for Nature Biomedical Engineering submission, July 2017) – Federal support is being acknowledged in this paper.

- **Books or other non-periodical, one-time publications.** *Nothing to report*

- **Other publications, conference papers, and presentations.**

Presentations – Invited
Brian W Pogue, "Novel Optical Contrast in Cancer: Cherenkov radiation in radiotherapy and in nuclear medicine" Invited Talk, Optical Society of America Biomedical Optics Topical Meetings, Miami FL, April 2016.

Conference papers published
Jinchao Feng, Petr Bruza, Hamid Dehghani, Scott C. Davis, and Brian W. Pogue, "Cherenkov-Excited Luminescence Sheet Imaging (CELSI) Tomographic Reconstruction" Proceedings of the SPIE BiOS, San Francisco CA, February 2017.

Petr Bruza, Huiyun Lin, Lesley Jarvis, David Gladstone, Brian Pogue, "Light sheet imaging with Cherenkov radiation for whole-body high-resolution functional luminescence recovery" World Molecular Imaging Society Annual Meeting, New York NY, Sept 2016.

Petr Bruza, Huiyun Lin, Lesley Jarvis, David Gladstone, Brian Pogue Light sheet imaging with Cherenkov radiation for whole-body high-resolution functional luminescence recovery" American Association of Physicists in Medicine, Annual Meeting, Washington DC, July 2016

Conference papers submitted:
Petr Bruza, Jinchao Feng, David Gladstone, Lesley Jarvis, Brian Pogue "Cherenkov sheet molecular imaging provides 100 um whole body spatial resolution" American Association of Physicists in Medicine, Annual Meeting, Colorado, July 2017

Petr Bruza, Jinchao Feng, David Gladstone, Lesley Jarvis, Brian Pogue , "Imaging high-resolution 3D distributions and kinetics of long-lived fluorophores in deep tissue" World Molecular Imaging Society Annual Meeting, Philadelphia PA, Sept 2017

- **Website(s) or other Internet site(s)** - *Nothing to report*

- **Technologies or techniques** – *Nothing to report*

- **Inventions, patent applications, and/or licenses** - *Nothing to report*

- **Other Products**

    We have produced mostly control software and analysis tools for CELSI. These are available to any researchers interested in them, and will be more widely distributed via our website in future years when they can be better packaged in a manner more appropriate for distribution.

7. **PARTICIPANTS & OTHER COLLABORATING ORGANIZATIONS**

- **What individuals have worked on the project?**

Name:	*Petr Bruza*
Project Role:	*Post Doctoral Researcher*
Researcher Identifier (e.g. ORCID ID):	*n/a*
Nearest person month worked:	*4*
Contribution to Project:	*Dr Bruza worked on CELSI data recovery and intial assessments of recovery,*

	deconvolution, and depth dependent attenuation correction. He is the lead on instrumentation development.
Funding Support:	*This award*

■

Name:	*Sarah Gollub*
Project Role:	*Post Doctoral Researcher*
Researcher Identifier (e.g. ORCID ID):	*n/a*
Nearest person month worked:	*3*
Contribution to Project:	*Dr Gollub worked on CELSI data acquisition for S/N analysis and spatial resolution testing.*
Funding Support:	*This award*

■

Name:	*Ethan LaRochelle*
Project Role:	*Graduate Student*
Researcher Identifier (e.g. ORCID ID):	*n/a*
Nearest person month worked:	*2*
Contribution to Project:	*Ethan has begun his phd work looking at spatial resolution achievable and testing oxygen sensitive phosphorescent nanoparticles which are taken up into cancer cells.*
Funding Support:	*This award*

■

Name:	*Jinchao Feng*
Project Role:	*Associate Professor*
Researcher Identifier (e.g. ORCID ID):	*n/a*
Nearest person month worked:	*3*
Contribution to Project:	*Dr Feng is a collaborator who used to be in our laboratory as a visiting scientist, with primary appointment at the Beijing Institute of Technology. He advises our work on the reconstruction algorithms.*
Funding Support:	*He has his own institutional funding for this collaboration.*

■

Name:	*Brian Pogue*
Project Role:	*Co-PI*
Researcher Identifier (e.g. ORCID ID):	*n/a*
Nearest person month worked:	*2*
Contribution to Project:	*Dr Pogue supervises all laboratory work on data collection, experimental design and analysis of results.*
Funding Support:	*This award*

■

Name:	*Lesley Jarvis, MD PhD*
Project Role:	*Co-PI*
Researcher Identifier (e.g. ORCID ID):	*n/a*
Nearest person month worked:	*2*
Contribution to Project:	*Dr Jarvis supervises all biological laboratory work on tumor choices and preparation for animal work and analysis of results.*
Funding Support:	*This award*

▪

Name:	*David Gladstone*
Project Role:	*Co-Investigator*
Researcher Identifier (e.g. ORCID ID):	*n/a*
Nearest person month worked:	*1*
Contribution to Project:	*Dr Gladstone supervises all radiotherapy access and work related to beam choices, scanning, machine use and scheduling, and interpretation of results.*
Funding Support:	*This award*

▪ **Has there been a change in the active other support of the PD/PI(s) or senior/key personnel since the last reporting period?-** Nothing to report

▪ **What other organizations were involved as partners?** – nothing to report

8. **SPECIAL REPORTING REQUIREMENTS**

▪ **COLLABORATIVE AWARDS:** *For collaborative awards, independent reports are required from **BOTH** the Initiating PI and the Collaborating/Partnering PI. A duplicative report is acceptable; however, tasks shall be clearly marked with the responsible PI and research site. A report shall be submitted to https://ers.amedd.army.mil for each unique award.*

The two reports will be uploaded with the same text, as the results are intimately related to one another, but the tasks for Jarvis and Pogue are clearly delineated in section 3 above.

9. **APPENDICES:**

Addressing overlap between this project and recently funded NIH grant R01EB024498-01

In terms of the concerns related to the new NIH grant, R01EB024498-01, there is no scientific overlap. I am enclosing a copy of the specific aims and you can see that they are quite different. The work in Aims 1 and 2 are focused around development of a deep tissue imaging system for whole body imaging of rodents, rather than just lymph node imaging which is fairly superficial. The detectors needed for the deeper tissue imaging are much more sensitive than that used for the CDMRP grant proposal. Additionally the Aim 2 of the R01 is focused on development of a stand alone system, such that it is not tethered to a clinical linac, but rather is used with a lone short pulse linac, not found in the clinic. This work is supporting Research Scientist Petr Bruza, as well as

The R01 Funding supports the system development for the R01 grant, which is just starting, as funding has been dedicated on August 1, 2017. The individuals funded to work on that R01 grant are PhD students Tengya Peng (who has not started yet, but begins next week) and Post doctoral student Mengya Jia PhD, who is focusing on a unique image reconstruction algorithm for distributed objects (not lymph notes) within thick tissue volumes.

This CDMRP aims are focused around system optimization and development for breast lymph node imaging, and we have completed a substantial amount of work on this. The system development for this CDMRP grant has been completed now, as described in our first annual report.

The CDMRP funding supports the individuals: post doc Sadie Gollub PhD (now finished her 9 month position and moved on), the final work of Alisha D'Souza a graduate student to summarize her work on two probe fluorescence sensing (she has now moved to another job after completing her PhD), the initial work of Research Scientist Petr Bruza PhD (who was funded and now shifted to another project, but developed the linear reconstruction approach for lymph node detection) and current post doc, Jennifer Shell PhD, who is finalizing the oxygen sensing probes assessments, and completing the planned in vivo imaging studies with the Biological Laboratory Technician Jason Gunn.

Cherenkov Excited Luminescence Scanned Imaging provides the highest resolution & molecular sensitivity for pre-clinical whole body imaging

Brian W. Pogue[1,6], Jinchao Feng[2], Huiyun Lin[1], Petr Bruza[1], Ethan LaRochelle[1], Rongxiao Zhang[1],

Hamid Dehghani[3], Scott C. Davis[1,6], Sergei Vinogradov[4], David J. Gladstone[1,5,6], Lesley A. Jarvis[5,6]

[1]*Thayer School of Engineering, Dartmouth College, Hanover, NH, 03755*
[2] *Faculty of Information Technology, Beijing University of Technology, Beijing, China, 100124*
[4]*School of Computer Science, University of Birmingham, Birmingham UK, B152TT*
[4]*Department of Biochemistry and Biophysics, Perelman School of Medicine, University of Pennsylvania Philadelphia PA 19104*
[5]*Department of Medicine, Geisel School of Medicine, Dartmouth College, Hanover NH 03755*
[6]*Norris Cotton Cancer Center, Dartmouth-Hitchcock Medical Center, Lebanon NH 03756*
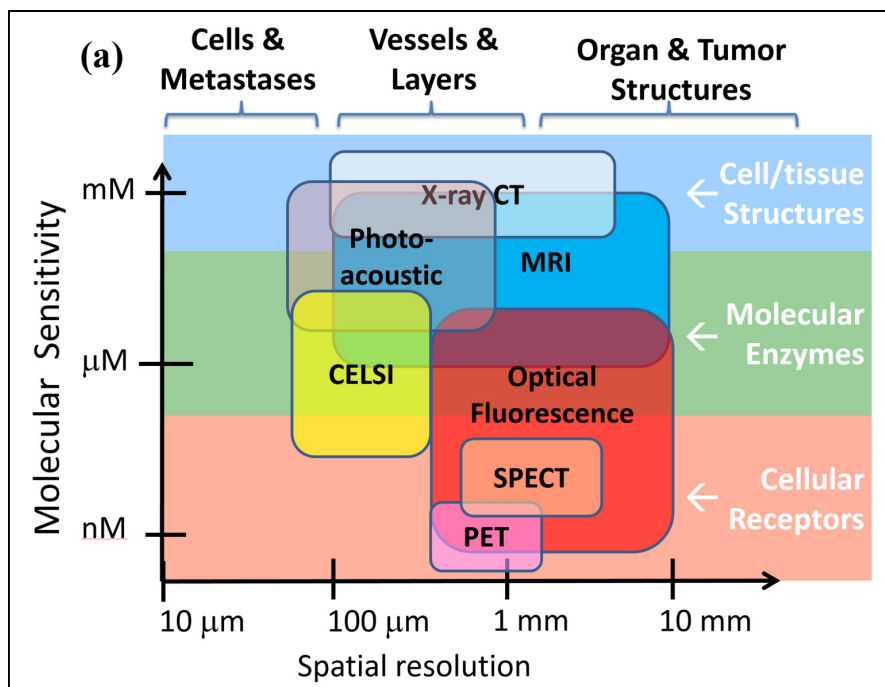
ABSTRACT

Molecular imaging with Cherenkov light excitation from external beam radiation is optimally achieved using an approach where a thin sheet radiotherapy beam is scanned orthogonal to a time-gated camera, such that luminescent emission is captured as remitted from the tissue. The reconstruction of the signal to the excitation volumes can provide 100 micron spatial resolution with a molecular sensitivity below the μM range in vivo. The performance limiting characteristics were beam size & scan geometry, typical probe concentration, radiation dose, and depth into tissue. The strengths of this imaging show that it could be the highest sensitivity and highest resolution optical imaging approach for molecular tracers in vivo.

Introduction

Molecular sensing of cells and tissue environment and physiology with optical luminescent probes is the most dominant imaging modality used today in both in vitro and in vivo research [1-3], as compared to x-rays, ultrasound, nuclear medicine or magnetic resonance imaging (MRI). Yet, optical imaging in vivo has fundamental limits imposed on the depth of penetration from optical elastic scattering in tissue [4-6]. While fluorescence and bioluminescence have been used extensively to elucidate intracellular signaling in hundreds of millions of studies *in vitro*, their use *in vivo* is largely limited to bulk temporal kinetics, surface organ or tumor imaging [7-9], or involving invasive/surgical measurements [7]. Tomographic optical imaging has been feasible in a number of research studies [10], but the nonlinear nature of the ill-posed reconstruction problem leads to very limited quantitative accuracy and repeatability, and few in vivo biological studies have relied upon this type of imaging. Thus, the ability to image luminescent molecular probes at high spatial resolution, *r*, in vivo has always been limited, even though the potential impact of this would be enormously beneficial for healthcare research. Methods such as photoacoustic imaging work well for absorbing molecular probes, but because of the nature of absorption-acoustic contrast, this works best at higher concentrations. The ability to probe the limits of tissue physiology at the metabolic and immunologic levels requires the need to sense concentrations at or below ⬚Molar concentrations in vivo. An illustration of the capabilities of this type of CELSI as an imaging tool in terms of sensitivity and spatial resolution, relative to other imaging systems today, is shown in Figure 1. In this study, a methodology to sense luminescent molecular probes deep within tissue is analyzed, which utilizes ionizing radiation induced Cherenkov emission, in a scanning sheet geometry, directly analogous to light sheet microscopy [11]. This geometry preserves the maximum contrast to background at the camera imaging, which tends to be the dominant factor in detectability and quantitative imaging studies.

The choice of optical molecular probes comes from the fact that they can match the biological size and molecular bond strengths of biochemical processes, ideally without distorting the tissue physiology [9]. While x-rays and microwaves can penetrate tissue even better than optical signals, they tend to have either higher toxicity or lower biological compatibility than small biochemical probes. The notable exception to this is isotope based imaging in nuclear medicine, where the radiolabel is integrated as a single atom into regular biological molecules [12], which provides exquisite imaging and largely complete integration with normal physiology. Nuclear medicine imaging of small animals is perhaps the gold standard for molecular imaging, and is limited by the interaction mechanisms to spatial resolution near one millimeter (see Figure 1) [13, 14], and suffers from higher cost and lower animal throughput. In general, imaging systems suffer from limitations in molecular sensitivity (y-axis of Figure 1) or in spatial resolution (x-axis of Figure 1). The type of imaging demonstrated with Cherenkov excitation of molecular optical signals has the potential for superior molecular sensitivity and spatial resolution as compared to other whole body imaging modalities.
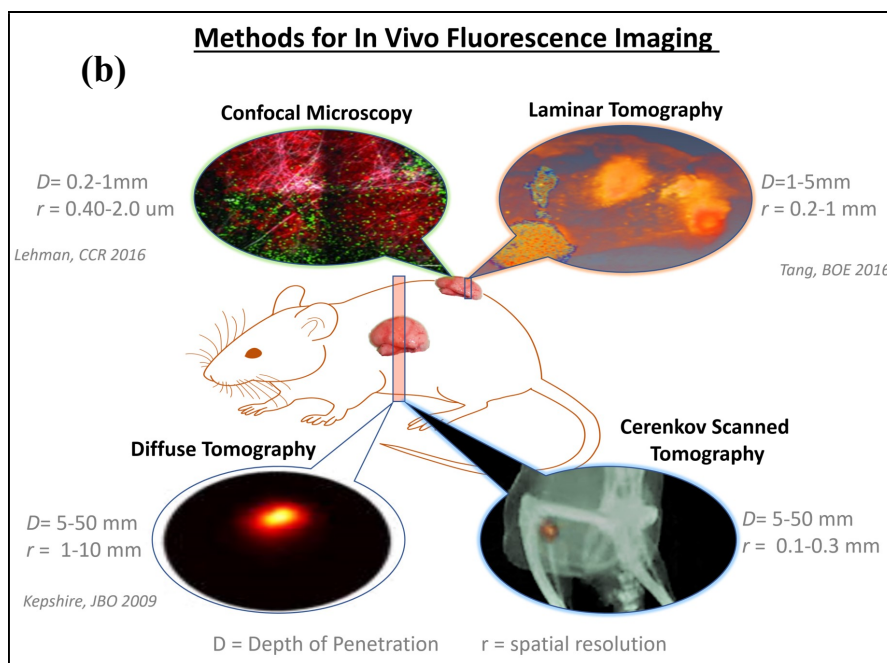
Methods for In Vivo Fluorescence Imaging

(b)

Confocal Microscopy
D= 0.2-1mm
r = 0.40-2.0 um
Lehman, CCR 2016

Laminar Tomography
D=1-5mm
r = 0.2-1 mm
Tang, BOE 2016

Diffuse Tomography
D= 5-50 mm
r = 1-10 mm
Kepshire, JBO 2009

Cerenkov Scanned Tomography
D= 5-50 mm
r = 0.1-0.3 mm

D = Depth of Penetration   r = spatial resolution

Figure 1. (a) shows an illustration of the characteristics where Cherenkov excited sheet luminescence imaging (CELSI) can achieve is shown relative to other whole body imaging modalities. The need for high spatial resolution with low molecular sensitivity provides the ability detect and image cellular metabolic and immunologic activities in vivo. In (b) the four major optical fluorescence imaging tools are shown with only diffuse tomography and CELSI being truly whole body imaging systems but diffuse tomography suffering from modest spatial resolution [15-17].

The spatial resolution in optical imaging can be diffraction-limited on surfaces, $r=\lambda/2NA$, defined only by the wavelength, λ, and the imaging system numerical aperture, NA, for microscopy, but in all deep tissue in vivo optical imaging approaches, the spatial resolution and signal strength degrade rapidly with increased depth into the tissue, such as in vivo confocal fluorescence microscopy or two photon imaging, which have a hard limit near D=1mm of useful penetration [18]. Imaging through D=2-3mm of tissue is done with laminar optical tomography, achieving r=100-200micron spatial resolution [19], as shown in Fig 1(b). Diffuse fluorescence imaging through an entire rodent is commonly done, but with r limited by the diffusion kernel, often quoted at 20% of the thickness ($r \approx 0.2$ D) [20]. This can be improved by informed approaches to regularization of the inverse reconstruction, or by spatial constraints applied by a secondary modality, however generally it is not feasible to do much better than the $r \approx 0.2$ D criteria. As such, an optical imaging tool which can preserve the linearity of the signal with depth, and not be affected by scatter dominance in tissue, will have better detectability with depth, illustrated in Fig 1(b). The example of photoacoustic imaging is a good illustration of a hybrid modality which uses sound to recover the signal induced by optical excitation, and therefore has superior depth of penetration and spatial resolution, as defined largely by the ultrasound. However, because the ultrasound signal is induced by absorption, the molecular sensitivity tends to be limited to micromolar concentrations. A modality which uses optical luminescence as the mechanism of contrast is inherently more sensitive because of the potential for single photon detection, and hence probing signals from molecular concentrations at the nanoMolar level in tissue.

Molecular imaging systems utility *in vivo* is largely determined by what is possible in terms of the chemistry of molecular probes. As shown in the color coding of the y-axis in Fig 1(a), achieving nM level sensitivity allows probing of cellular immunology events such as antibody binding and antigen expression, whereas systems which probe at the micromolar level can only hope to image cellular and tissue metabolites such as enzymes and physiological minerals. As such, there is enormous value in developing systems to probe nM concentration levels, as are commonly used in nuclear medicine imaging studies.

Cherenkov light is emitted in tissue from the high energy x-rays due to Compton-scatter induced secondary electrons that interaction with the dielectric media, when above the threshold energy ≈220keV. Unlike optical radiation, which is strongly scattered in tissue, therapeutic megavoltage (MV) LINAC x-rays do not experience significant scattering, as shown in Fig. 2(b) relative to the optical excitation illustrated in (a). So, while there is a build-up region in tissue of

secondary electrons, the Cherenkov intensity from 18 MV photons can be relatively uniform over several centimeters. LINAC beams are pulsed at 360 Hz with a 3-4us pulse length, as illustrated in Fig 2(d), allowing the use of a time-gated intensified CCD (ICCD) camera for detection of the exiting luminescence from the tissue [21, 22], where the lifetime of the emission is longer than the linac pulse. as illustrated in Figure 2(c) with the linac beam vertical, cone beam CT lateral and camera view angle slightly off vertical. The spectrum of Cherenkov is broadband and peaked in the UV, and decays in intensity, I, with a wavelength dependence of $I \sim 1/\lambda^2$, as shown in Fig 2(e). However, the UV-blue-green spectral range has a very short diffusion path (<0.1mm) in the tissue due to the absorption from hemoglobin. Therefore, luminescence of the probe is excited only with the volume that is directly in the path of the scanning radiation beam. This property constitutes the key aspect of the Cherenkov excited luminescence sheet imaging (CELSI) scheme, which is that all luminescence signals detected by the ICCD originate exclusively along the pathway of the LINAC beam, as shown in Fig. 2.

Deep tissue excitation with Cherenkov light from ionizing radiation from isotopes has been demonstrated to excite molecular fluorescence [23, 24], with the signal increasing with emitted gamma ray energy. Similarly radiation delivered by a medical linear accelerator (LINAC) generates Cherenkov emission within the treated tissue[25] and has been visualized for patient dosimetry studies [26] as well as excitation of molecular probes[22, 27]. This process can be utilized to excite fluorescent or phosphorescent probes within the tissue to diagnostically sense molecular features, and has been demonstrated at low radiation doses [28] utilizing high energy (18 MV) photons which have the highest generation of Cherenkov with the lowest deposited dose level in tissue. While this tool has interest, perhaps the most important aspect of the approach is that it can be used in geometries which mimic those of microscopy, taking advantage of some of the principles of directed excitation imaging tools such as ultrasound. The excitation light from Cherenkov is directed by the incident beam, and so the observation of emission need not be highly localized if the signal is back-projected along the line of the Cherenkov beam, and attenuation correction can be readily applied to the signal based upon the depth of imaging. Additionally, altering the orthogonality of the excitation and emission beam allows some advantages in signal to background improvement, as is demonstrated here and used in thick tissue fluorescence microscopy.[11, 29] These key principles make this approach to signal measurement much more useful for whole body imaging, as is demonstrated in this study.
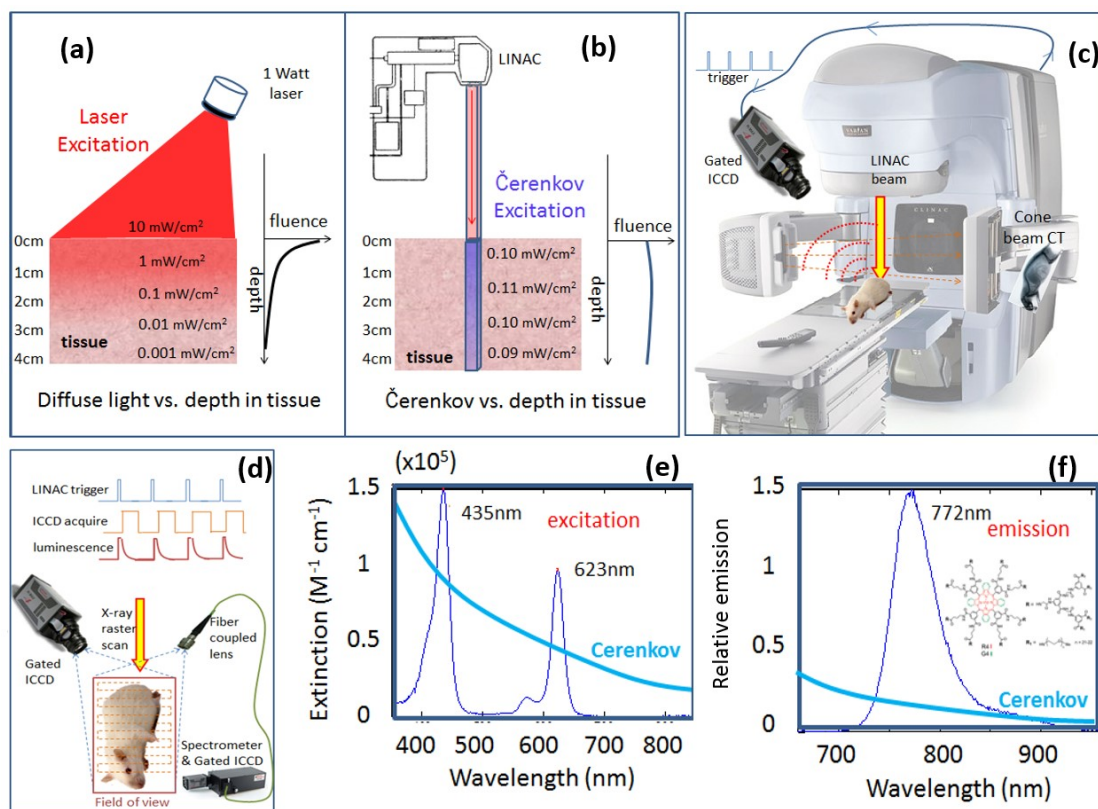

Figure 2. A comparison of the excitation fluence decay with depth into tissue for (a) laser/LED excitation and (b) Cherenkov excitation generated within the tissue from a LINAC radiation beam. The diagram of the experimental setup is shown (c) with measurement devices. In (d) a raster scan approach to image measured by the ICCD is shown with gated emission detected by a spectrometer system. In (e) the

absorption and (f) the luminescence emission spectra are shown for Oxyphor PtG4, with peak wavelengths labeled, and overlaid with the Cherenkov spectrum (blue). The insert in (f) is the structure of PtG4.

Results

Beam Size: By measuring total luminescence signal and considering prior information about position of the scanning beam, the distribution of optical signal along the direction of scanning can be recovered. In Fig 3 (a)-(c), the possible beam geometries are illustrated, where the x-ray sheet can be shaped as a broad beam, as is commonly used in radiotherapy, or a 2 dimensional sheet, or a pencil beam which can be raster scanned. The impact on the dose rate, spatial resolution and imaging time are all listed. The benefit of a pencil beam would be the highest spatial resolution, whereas the benefit of a broad sheet is the fast imaging acquisition. However, the choices here make a large impact on the image quality.
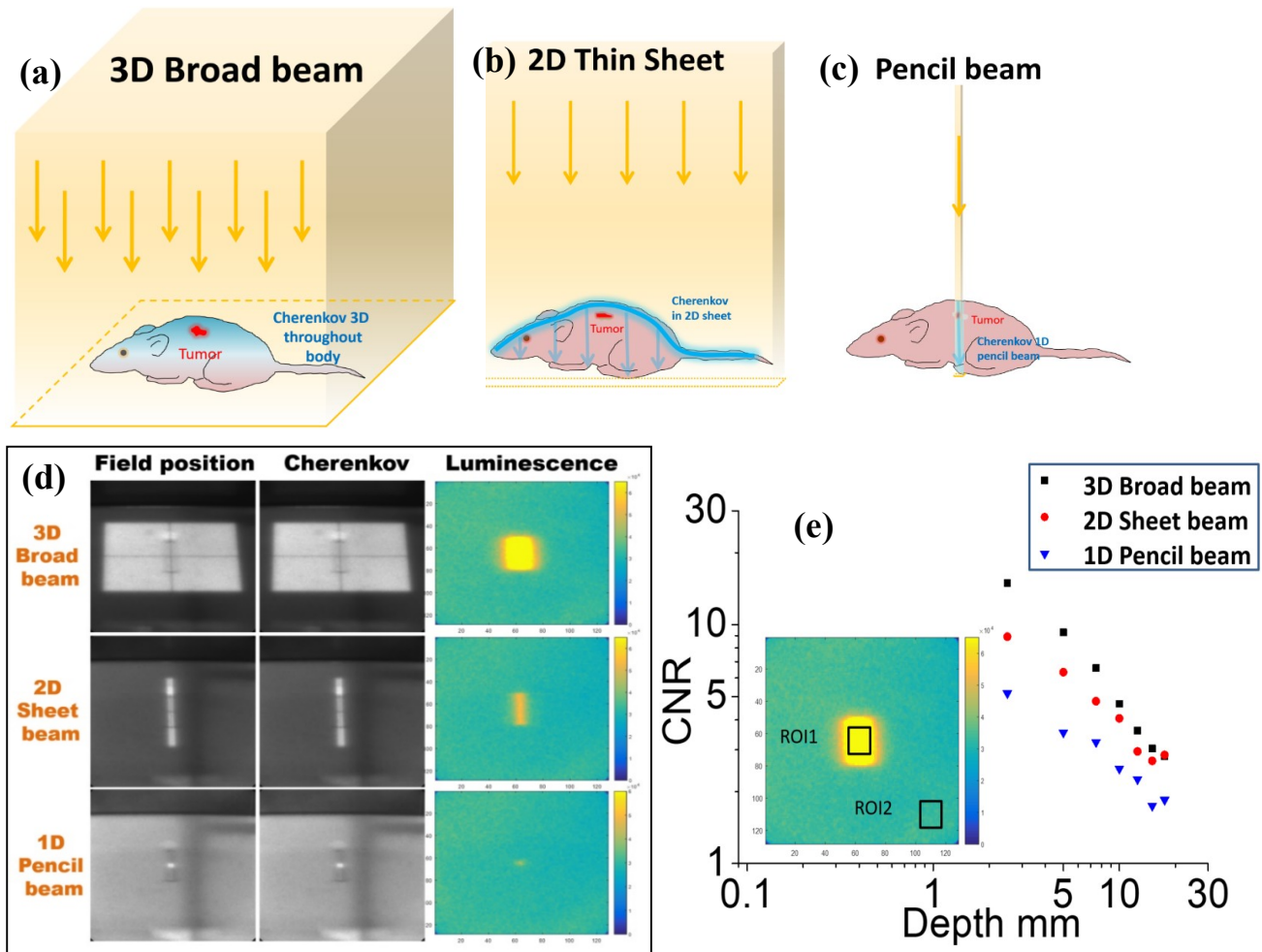

Figure 3 The configuration of the radiation beam shape and region of the tissue where Cherenkov would be generated by a (a) single broad beam throughout the 3D volume of the animal, or (b) in a 2D sheet beam, or (c) in a 1D pencil beam. These geometric choices each affect the signal to noise possible with CELSI, and hence the sensitivity of other parameters such as minimum concentration and depth of imaging feasible and acquisition time. Images of the field light, Cherenkov emission on a phantom and the luminescence from a single square target in the phantom are shown in (d) for the geometries in (a)-(c). The contrast to noise of the target relative to the background is shown in (e).

Imaging Geometry: When, controlled by the rotational gantry and the positions of the treatment bed, radiation beam energies are carefully chosen to reach specific depths in the body, and a set of beams from different gantry angles can be delivered to the patient from these planned entrance positions as shown in Fig 4(a) & (b) where the beam could be roughly orthogonal to the camera direction, for a sheet-like imaging, or aligned along it, for epi-illumination. The experimental set up was photographed, and is shown in (c) and (d), and a single image of a capillary at 5mm depth into a tissue phantom solution is shown for each geometry in (e) and (f), respectively. The colorbar for each is the same and so the significantly higher background near 10,000 counts, leading to a contrast of 1.2 is seen for the epi-illumination while the lower background near 2000 counts is seen for lateral illumination, leading to a contrast near 4.0. Because of this observation, the lateral excitation geometry was used throughout most of the next experiments.
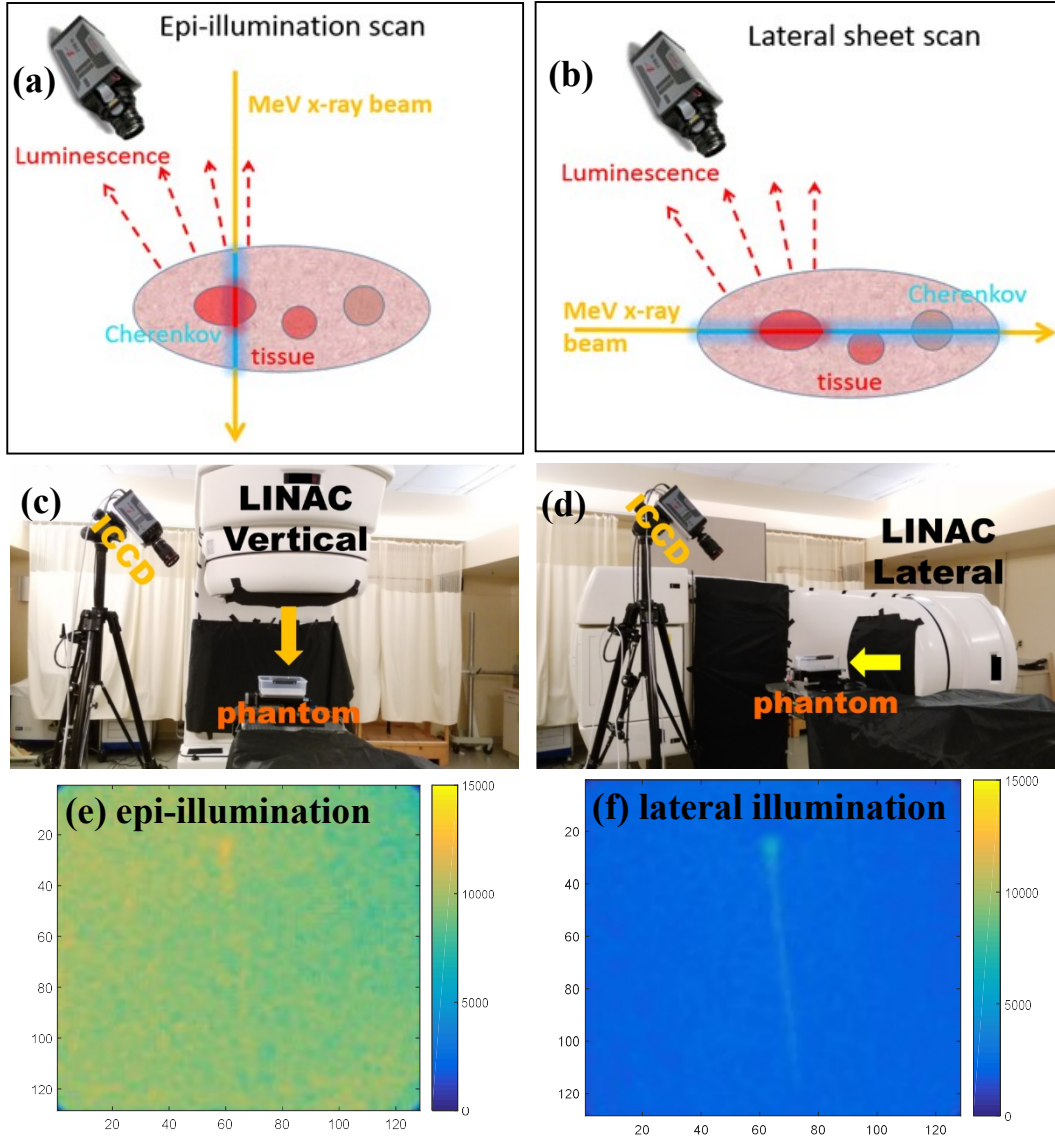

Figure 4. The geometry of imaging camera relative to X-ray beam entrance position is shown in (a) an epi-illumination scan, and (b) a lateral sheet scan. Photographs of the LINAC-camera set up for (c) epi-illumination and (d) orthogonal camera and linac beam. Images of PtG4 luminescence from a single capillary within a tissue phantom are shown in (e) and (f) for these geometries, respectively, illustrating the high background and hence poorer contrast from the epi-illumination geometry.

Dose, Concentration & Depth of Imaging: The dominant factors affecting image recovery were explored systematically by varying one parameter at a time. The contrast to background ratio was used as a metric of success, assessing how this varied with radiation dose delivered, concentration of PtG4 and depth of the object into the medium. CELSI of PtG4 in a 1mm diameter capillary was assessed with different concentrations, depths (distance from capillary to phantom surface) and radiation doses. First using a fixed depth of 5mm, the concentrations range was varied logarithmically from 500 mM down to 0.78 uM measuring contrast to background ratio for a 1 second acquisition time. The results are shown in Fig 5(a), being monotonic in shape and reducing to a contrast to background ratio of 1 at about 2 μM. Next the CBR was tracked for a fixed concentration of 50 mM, varying the depth down to 20mm into the phantom. This was monotonic with depth and appears to decrease near CBR=1 well beyond the 20mm depth. Finally the variation with radiation pulses

added together was studied at a target depth of 5mm and fixed concentration of 50 mM, showing monotonic dependence on dose, and decreasing to CBR of 1 at 2 radiation pulses, roughly equivalent to 0.06 cGy dose.
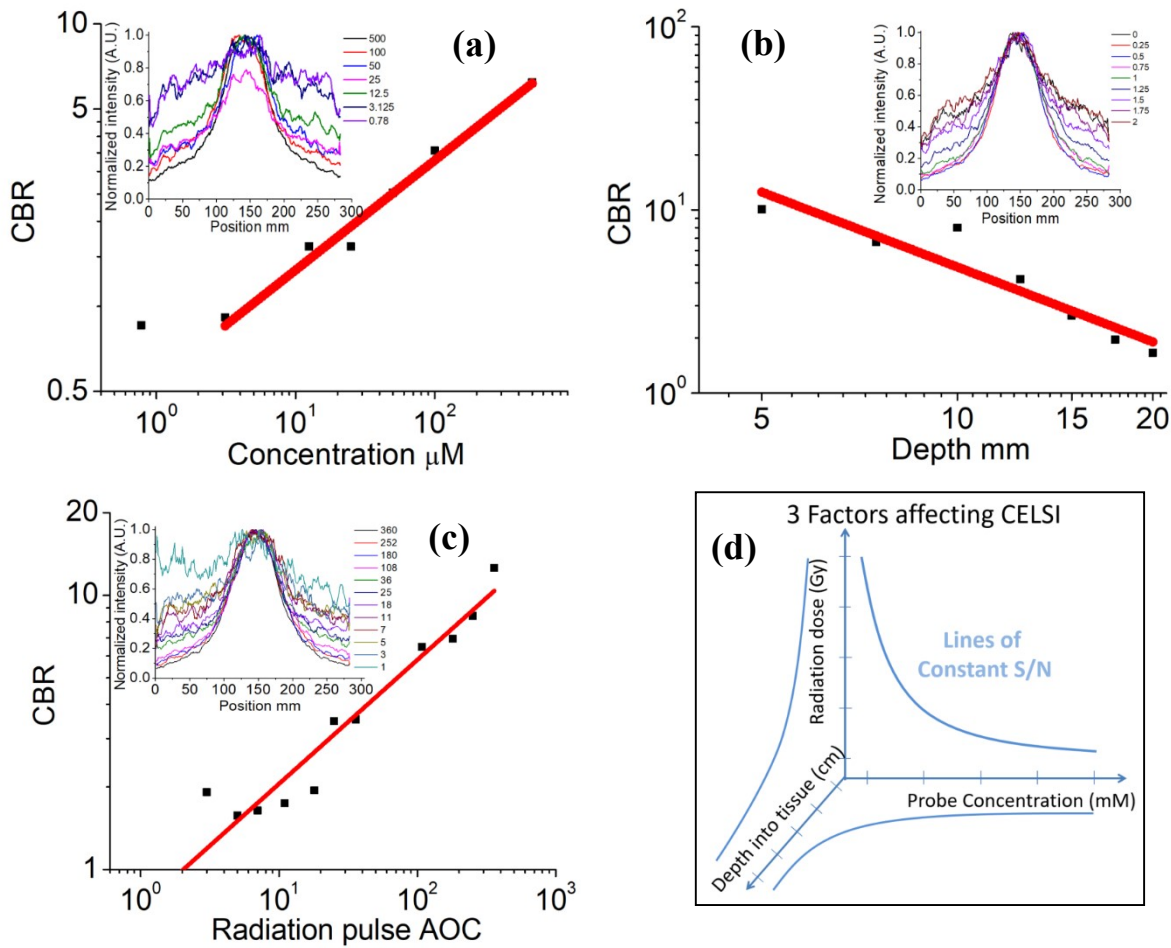

Figure 5. Contrast to Background Ratio (CBR) measurements from PtG4 contained within a 1mm capillary with (a) different concentrations in the physiologically relevant range, (b) varying depth between the capillary wall to the surface of the phantom being imaged, and (c) varying radiation dose between 1 and 500 radiation pulses.

Scan Directions and Tomographic Reconstruction: The direction and range of scan parameters in CELSI is quite large and three particular geometries were examined as analogous to other tomographic systems, and also to compare to fluorescence tomography systems. First a study of fluorescence tomography as acquired in the epi-illumination geometry was completed, as well as transmission geometry. These are shown in Figure 6(a) and (b) respectively with the test object shown, and reconstructed images in (d) and (e). The CELSI tomography image with lateral excitation and vertical detection is shown in the schematic (c) and reconstructed object in (f). In this case, CELSI is shown to be far superior to epi-illumination fluorescence tomography and higher contrast than transmission based fluorescence tomography.

Next the range of possible scans available with CELSI was explored on how it would affect image recovery. As shown in Figure 6(g)-(i), the horizonal, vertical and diagonal aspects of a scan can more fully interrogate the image space, and reconstructed images for these three respective geometries are shown in (j)-(l), with recovery from the combination of all of them shown in (m). From these simulations it is obvious that the excitation line directions distort the recovered objects, but as with all tomography applications, the larger the range of angles sampled, the better the image recovery can become, as shown in (m).
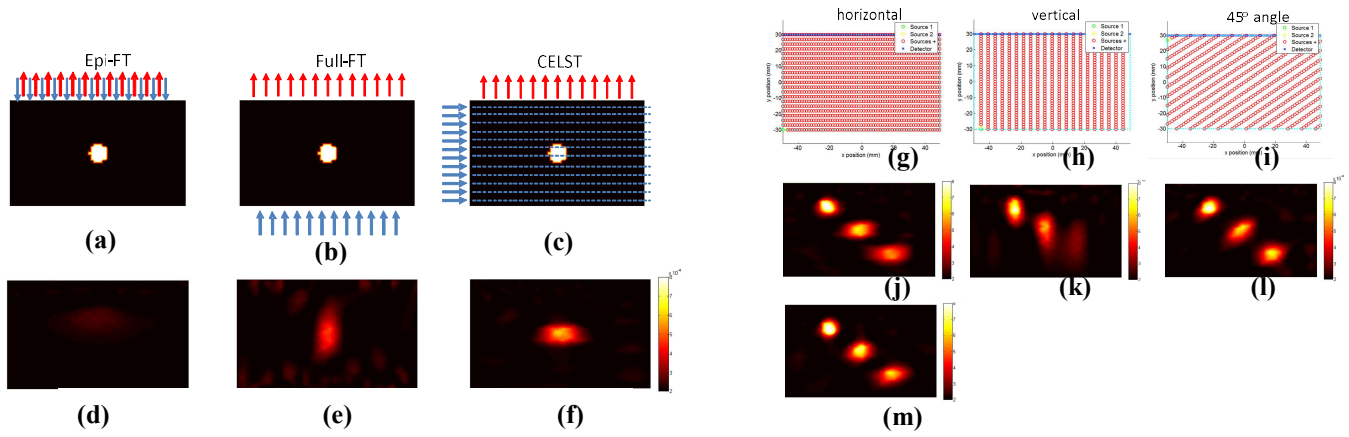
Figure 6. Source and detector placement used for (a) the Epi-fluorescence tomography (Epi-FT), (b) the Full-FT, and (c) the lateral excitation CELSI with tomographic reconstruction. The blue arrows represent the source locations, and the red arrows denote the detector locations. Reconstructed luminescence distributions corresponding to the three geometries shown in Fig 2(a)-(c), for (d) the Epi-FT, (e) the Full-FT, and (f) the CELST. Three angles of scanning for CELSI were examined as illustrated in (g) – (i), for horizonal, vertical and diagonal, respectively, and three test objects at different depths were used as a test field for this, with reconstructions as shown in (j) – (l). The combined set of all 3 scan geometries was used for the reconstructed image (m), showing the best preservation of the three objects space and intensities.

Spatial Resolution: Both experiments and simulation studies were completed to assess the ultimate limits to spatial resolution with optimized conditions. Simulation studies were carried out with varying depths and using a standard resolution test, varying the distance between two small objects as illustrated in Fig 7(a). The results reveal that when the depth of inclusions was smaller than 5mm, the CELST has the ability to discriminate the two inclusions with edge-to-edge distance of 0.1 mm, as plotted in (b). When the depth of inclusions was increased to 2.5cm, the two inclusions can be also discriminated with edge-to-edge distance but nearer 0.5 mm. When the depth of inclusions was increased to 3 cm, the two inclusions can be also discriminated with edge-to-edge distance but nearer 1.8 mm. The results show that CELST can yield high spatial resolution, but that this spatial resolution does degrade with depth into the medium, as would be expected. These CELSI results can be compared to Epi-FT and Full-FT results which have significantly lower spatial resolution (b), ranging from a few millimeters to beyond 10mm at depth of 15 and 25 mm into the medium. Fig. 7(a) shows the minimum spatial resolution as a function of depth of inclusions. Epi-FT could not reconstruct the inclusions accurately when the depth of inclusions was deeper than 15 mm, therefore, the spatial resolution was not calculated.

Experimental studies were carried out to try and match the simulations but using a simpler geometry of a single capillary rod, positioned at 5mm into the tissue simulating phantom medium. A range of capillaries with diameters varying from 1mm down to 0.1mm were used with PtG4 at 50 μM filled in them. The FWHM recovered was extracted and the observed FWHM is plotted against the true value in (d), showing nearly perfect linearity and matching the expected value of the smallest spatial resolution tested of 100 microns.

Last, a series of experiments to reconstruct an inclusion with a small size were performed. A single inclusion with 1 mm diameter was placed with increased depth of 1 mm (1 mm-60 mm). The fluorophore absorption coefficients for background and inclusion were set as zero and 0.008 mm^{-1}. The representative results for the recovered distribution of fluorescence yield are depicted in Figs. 10. The results indicate that the reconstructed size and yield degrade with increasing depth. However, the reconstructed centroid location of the inclusion appears to be accurate. The mean error in centroid recovery was found to be 0.3 mm over the range of 0-10mm. When the inclusion was adjust to a depth greater than 10 mm, quantitative accuracy was degraded; the mean error in the centroid recovery increased to 0.41 mm in the range of 1-30mm. The mean error in the centroid recovery was 0.43 mm in the range of 31-60 mm. Fig. 10(f) shows the errors between the recovered and true centroid locations with the depth increased from 1 to 60 mm, the FWHM of the recovered yield was also plotted in Fig. 10(g). Again, the CELST demonstrates its outstanding ability to accurately reconstruct a small inclusion with promising image quality.
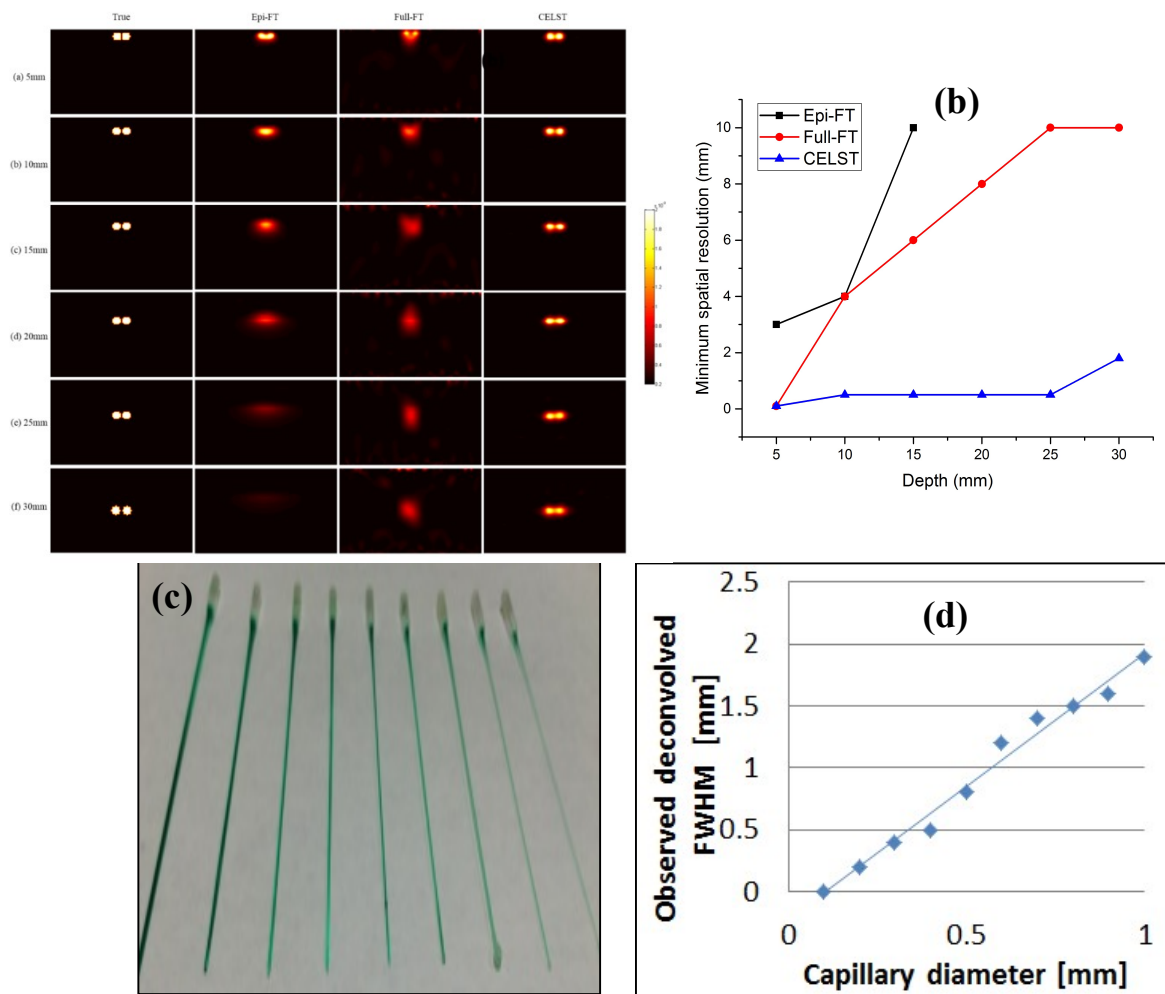
Figure 7. Capillaries filled with PtG4 are shown (a) and were embedded into a tissue equivalent phantom, and a sheet beam scanned laterally to extract the FWHM for each sized tube (b). To establish the theoretical limits to spatial resolution, reconstructed results using the CELST for two inclusions with varied edge-to-edge distance in different depths are shown, (c). For each depth the minimum resolvable distance was estimated and plotted in (d), for both diffuse fluorescence tomography, epi-illumination fluorescence tomography and CESLI tomography.

Rodent Imaging: In order to verify that imaging in a complex tissue shape would be possible, the Xf2-m phantom was imaged with 50 uM PtG4 in the cylinder, inserted into the central part of the body. The remitted luminescence image from above is shown in Fig 8(a) with the Cherenkov beam in the plane of the tube. This signal is super imposed on the white light image of the mouse phantom. Reconstruction of the emission was done with CESLI data, scanned in 0.1mm steps in the lateral beam direction. Reconstructed images are shown in the 3 orthogonal directions superimposed on CT scan images of the phantom (in grey scale). This recovery shows good localization and recovery of the shape as might be expected, shown in Fig 8(b).

To further advance and test the performance of the CELSI reconstruction, an in vivo experiment with a tumor-bearing mouse was performed. The mouse was injected with 10 nmols of PtG4 and imaged within 1 hour of injection. The other experimental setting was same as the phantom experiment. Fig. 8(c) shows the CT scan of the animal, and (d) shows the acquired luminescent Maximum Intensity Projection image overlaid on the color coded CT scan. The CT images were used to generate a finite element mesh, and the optical properties of tissues in the mouse were estimated by average homogeneous values for a mouse, based upon published values [17]. The regularization parameter used in reconstruction was 10. Fig 8(e) (f) and (g) show the 3D CELST reconstructed results from the 3 orthonal views of the body interior, with reconstructed CELSI

23

data in red. The tumor can be located accurately, and the recovered size is substantially smaller than a diffuse tomography system image.
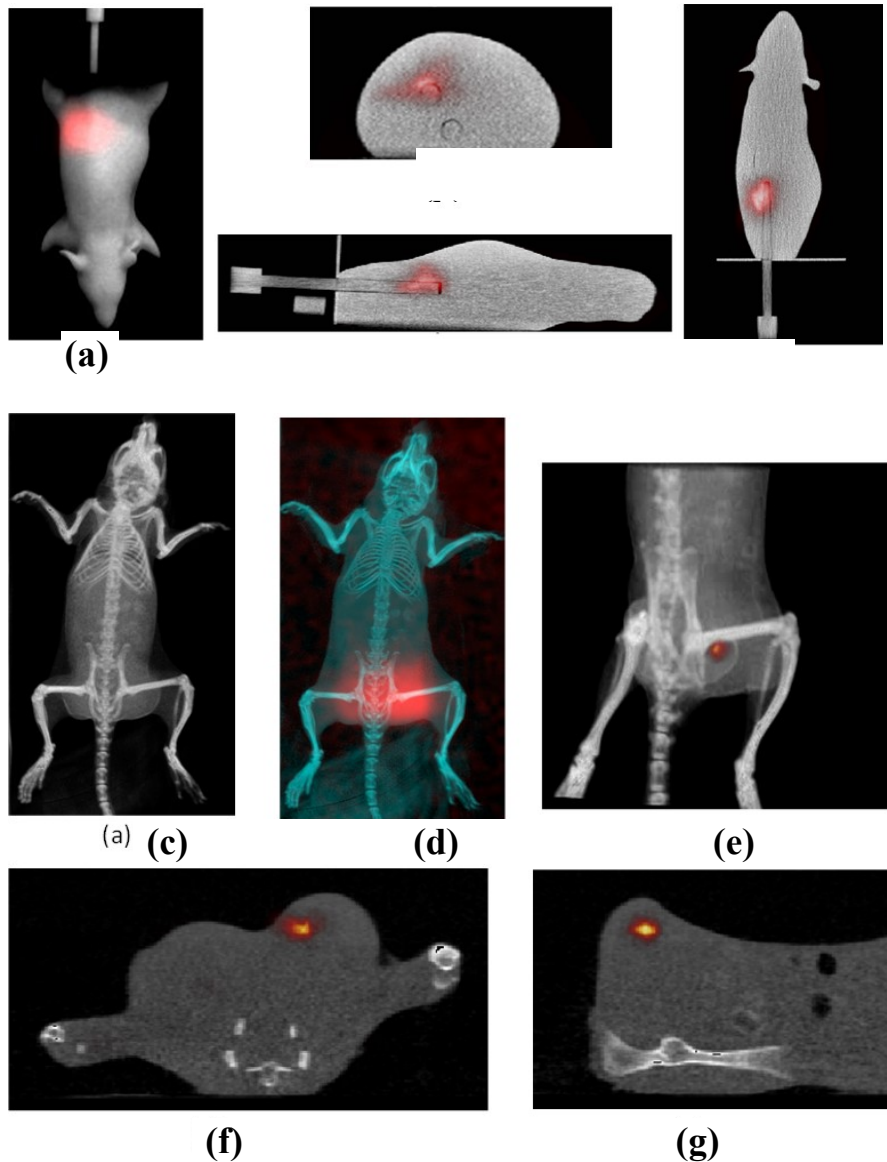

Figure 8. The phantom experiment. (a) The luminescent images overlaid on the top surface of the CT images; (b) are the reconstructed images shown with 3 orthogonal views, coronal, sagittal and transverse. The in vivo imaging study is shown with an x-ray CT scan (c), and a MIP image of the luminescence overlaid on the color-coded CT scan (d). Then CELSI tomographic data is overlaid on the three orthogonal CT images for oblique (e), coronal (f) and sagittal (g) views of the reconstruction.

Discussion

Optical imaging of tissue has the potential for such rich molecular information, but has been plagued by the scattering of light in tissue, making the signal non-linear and affected by tissue shape, optical properties, layers and regions, and often unacceptably low signal to noise with any appreciable depth into the tissue. CELSI is proposed here as a way to directly use high energy radiotherapy beams to launch light directly into the tissue, and by the knowledge of where the light was placed, it can allow high resolution recovery of luminescent sources. While this approach to imaging has been introduced in just the past two years [28, 30], the factors that dictate the performance have not been exhaustively analyzed and non-linear tomography has not been applied to fully vet the imaging contrast recovery and spatial resolution. In this study, these issues have been fully examined and the capabilities of this type of imaging can now be established.

The beam shape and angle of orientation have perhaps the largest effects upon the signal, with larger beam shapes having substantially larger signals, presumably based upon the fact that the light scatters and builds up within the tissue. Additionally, there is an output factor for the beam which reduces with smaller beam sizes as well, and so while smaller or thinner beams provide the best spatial resolution, as shown in Fig 3, they inherently provide the lower signal intensities as well. The direction of the beam relative to the camera, has perhaps the second most important factor, as a separation of the source from the surface being imaged inherently improves the observed contrast, as illustrated in the images of Fig 4. For these reasons, much of the work following these two initial studies focused around using the lateral beam geometry predominantly, and with a wide sheet of radiation, to maximize build up and light irradiance in the tissue.

Testing the key performance factors beyond these initial choices leads to a complex array of possible parameters. The radiotherapy dose, the probe concentration and the depth into the tissue each contribute to the detected signal in ways which would have a reciprocity, as illustrated in Fig 5. The imaging of luminescent targets is possible within the range of concentrations, doses and depths which are suitable for small animal imaging. The concentration ranges of μM to slightly below a μM is typical for metabolites and higher concentration receptors, and the ability to resolve uptake within many millimeters of tissue is a very important application in pre-clinical imaging. Radiation doses used here have been in the range of x-ray exams, so while the concept of using a linear accelerator for imaging appears dangerous from a radiation safety perspective, it is critical to appreciate that this is done with very little dose delivered.

Perhaps the key observation in this work has been establishing the feasible spatial resolution several millimeters into the animal tissue. This spatial resolution is largely dictated by the precision in which the x-ray beam can be controlled, because in the end the signal origin can be localized to where the beam excited the luminescent agent. The imaging tests both experimentally and computationally support the believe that the spatial resolution is in the range of 100-300 microns for objects as deep as 5mm into the tissue. Computationally this spatial resolution appears to be resolvable down to 20mm deep, and this fundamental limit is a fascinating goal for deep tissue imaging, essentially being able to achieve near microscopic resolution deep into tissue with optical imaging.

Finally, the tests demonstrated here of mouse phantom and a mouse tumor, in Fig 8, demonstrate the localization concepts and how the accuracy of reconstruction is far superior to diffuse tomography or superficial MIP images of luminescence. This latter comparison is important, because the vast majority of pre-clinical luminescent imaging is done with epi-illumination box systems where a single superficial surface image of the animal is achieved. Being able to bring optical imaging to a significantly higher whole body spatial resolution would have a profound impact for molecular imaging.

Outlook

This study has extensively demonstrated the key parameters and capabilities of Cherenkov Excited Luminescence Scanned Imaging (CELSI) detailing the spatial resolution possible in the hundreds of microns, while utilizing micromolar concentrations of an oxygen sensitive biological probe. The Cherenkov was excited by x-ray beams from a linear accelerator which can be shaped into thin sheets and scanned in arbitrary directions. The time-gated luminescence is captured and with a combination of scan beam positions, recovery of high resolution emission images is possible, using radiation doses equivalent to that of a diagnostic x-ray imaging session. The depths and recovery possible are suitable for small animal imaging studies. Agreement between both computer simulation and experimental recovery suggests that when fully automated, this type of imaging will have one of highest sensitivities and spatial resolutions for any pre-clinical whole body optical imaging system.

Methods

LINAC & Cherenkov Imaging: Cherenkov was induced by a linear accelerator (Varian Linac 2100CD, Varian Medical System, Palo Alto, CA) based at the Norris Cotton Cancer Center, at Dartmouth-Hitchcock Medical Center. The LINAC multi-leaf collimator (MLC) provided high flexibility in shaping the output beam to make arbitrary shaped treatment fields. Leaves are typically 5mm wide and oriented in many long thin sheets that are controlled to move in and out of the output beam, and can be controlled to a level of 0.1mm precision. The effect of beam shape on the signal to background recovered acquisition was studied with radiation beam sizes using a larger square beam 40×40 mm^2, a thin sheet beam of 5×40 mm^2, and a thin square pencil beam 5×5 mm^2. Each of these were studied for epi-illumination imaging and then the thin sheet beam was also used for lateral sheet excitation, as will be shown, for optimal contrast.

Luminescent Reporter & Tissue Phantoms: NIR fluorescent phosphorescent probe PtG4 Oxyphor [31] was prepared in the standard PBS at 500 µM concentration. The tissue simulating phantoms were prepared using 1% Intralipid© (Fresenius Kabi, Uppsala, Sweden). A capillary with 1 mm diameter of the probe at concentrations from 0.75 to 500 µM were placed inside the phantom at a depth which was varied between 2.5 to 20 mm from phantom surface being imaged. To study the dose efficacy for CELSI, the capillary containing the solution of the probe was irradiated with doses which varied from 360 pulses (approx. 10cGy) down to 1 pulse (approx. 0.06cGy) at 50 µM concentration and 5 mm depth.

Luminescence Imaging: The imaging system consisted of a time-gated intensified CCD camera (ICCD, PI-MAX4 1024i, Princeton Instruments, USA), a commercial lens (Canon EF 135mm f/2L USM,) and a tripod mounted approximately 1 m from the target. The camera was focused on the PtG4 capillary (1 mm diameter). The time-gated ICCD camera was synchronized to the radiation pulses (approximately 3.25 µs duration, 360 Hz repetition rate) with the intensifier set as ×100 and turned on at a 3.5 µs or 500 µs gate delay following each radiation pulse for phosphorescence or background measurement, and luminescence generated during 50µs gate width was integrated via this ICCD.

Factors Affecting Contrast: Dose, Concentration, Depth: The signal contrast in all imaging systems is a function of key parameters and so for CELSI it was hypothesized that these key factors would be linearly related to the radiation dose used, the concentration of probe present in the tissue, and the logarithm of the depth in which the target was located. The depth dependence on signal is likely more complex because of the light diffusion process, but might be expected to fall off over macroscopic distances with the effective attenuation coefficient of the medium, estimated by diffusion theory to be $\mu_{eff} = (3\mu_a\mu_s')^{1/2}$, where μ_a is the absorption coefficient and μ_s' is the transport scattering coefficient of the tissue. The dose delivered was varied by simple linear summation of the signal over more linac pulses, to effectively build up signal with delivered dose. The concentration of PtG4 was varied in solution within the embedded object, from 500 µM down to 0.78 µM.

Spatial Resolution Assessment: The spatial resolution of imaging was assessed with a range of capillary tubes placed into tissue simulating phantom at 5mm depth, and the sheet beam was scanned laterally across the tube, to vary the signal with position. The capillaries were filled with 50 uM PtG4 to provide a high contrast target for resolution assessment, and the recovered full width at half maximum (FWHM) was recovered for each capillary.

Computed Tomography Recovery: CELSI data can be scanned for different beam angles and the performance expected varies considerably based upon these choices. The range of options is so large that experimental study of these is prohibitive, and so a series of computer simulations were carried out, in particular to compare CESLI images to diffuse fluorescence tomography images where tradiational light excitation is used as compared to Cherenkov excitation. Additionally, different combinations of scanning angles and different depths and sizes of objects could be simulated much more quickly than carrying out all the experiments. The computer simulations were carried out in the NIRFAST software package, used to model light transport in tissue, and carry out regularized iterative reconstruction of the luminescent reporter in the medium. To assess spatial resolution of CELSI tomography, a classic resolution test was performed with two small inclusions and varying the spatial distance between them, and assessing when the could no be resolved as separate objects. The edge-to-edge distance was varied from 0.1 mm to 5 mm, in the plausible range of limiting spatial resolutions given the physical constraints of the linac MLCs used. The yield contrast of inclusion was set as 10:1. A finer mesh with 6161 nodes and 12000 linear triangular elements was used in reconstruction. Inspired by the results of combining of scan modes, the following reconstructions were performed by summing up scan modes.

Animal phantom Imaging: In order to assess performance in a more complex tissue geometry, a commercially available mouse phantom was used (Xfm-2, PerkinElmer, Inc., Waltham MA), using rod of material inserted which was filled with 50 uM PtG4. The CELSI imaging was carried out with lateral beam excitation and vertically oriented emission capture, using a long lifetime gate on the camera, to sync out the Cherenkov light and noise, and maximize luminescence emission detection.

Animal Imaging: All animal procedures were approved by the Dartmouth Institutional Animal Care and Use Committee, and the studies here were carried out in compliance with these approved procedures. Briefly, an AsPC-1 cells were incubated in tissue culture media, and 10^5 cells were injected under the skin on the flank of a nude mouse. After 3 weeks of growth, an 8mm tumor was observed and the animal used for imaging. Under general anesthesia of inhaled isofluorane, 0.5ml of PtG4 was directly injected into the tumor and the animal was imaged by CT scan as well as CELSI.

Acknowledgments

Author Contributions

References

1.	Hoebe, R.A., C.H. Van Oven, T.W. Gadella, Jr., P.B. Dhonukshe, C.J. Van Noorden, and E.M. Manders, *Controlled light-exposure microscopy reduces photobleaching and phototoxicity in fluorescence live-cell imaging.* Nat Biotechnol, 2007. **25**(2): p. 249-53.

2.	Brismar, H. and B. Ulfhake, *Fluorescence lifetime measurements in confocal microscopy of neurons labeled with multiple fluorophores.* Nat Biotechnol, 1997. **15**(4): p. 373-7.

3.	Nie, S., D.T. Chiu, and R.N. Zare, *Probing individual molecules with confocal fluorescence microscopy.* Science, 1994. **266**(5187): p. 1018-21.

4.	Zipfel, W.R., R.M. Williams, R. Christie, A.Y. Nikitin, B.T. Hyman, and W.W. Webb, *Live tissue intrinsic emission microscopy using multiphoton-excited native fluorescence and second harmonic generation.* Proc Natl Acad Sci U S A, 2003. **100**(12): p. 7075-80.

5.	Bjorn, S., V. Ntziachristos, and R. Schulz, *Mesoscopic epifluorescence tomography: reconstruction of superficial and deep fluorescence in highly-scattering media.* Opt Express, 2010. **18**(8): p. 8422-9.

6.	Georgakoudi, I., B.C. Jacobson, J. Van Dam, V. Backman, M.B. Wallace, M.G. Muller, Q. Zhang, K. Badizadegan, D. Sun, G.A. Thomas, L.T. Perelman, and M.S. Feld, *Fluorescence, reflectance, and light-scattering spectroscopy for evaluating dysplasia in patients with Barrett's esophagus.* Gastroenterology, 2001. **120**(7): p. 1620-9.

7.	Mittapalli, R.K., V.K. Manda, K.A. Bohn, C.E. Adkins, and P.R. Lockman, *Quantitative fluorescence microscopy provides high resolution imaging of passive diffusion and P-gp mediated efflux at the in vivo blood-brain barrier.* J Neurosci Methods, 2013. **219**(1): p. 188-95.

8.	Leblond, F., S.C. Davis, P.A. Valdes, and B.W. Pogue, *Pre-clinical whole-body fluorescence imaging: Review of instruments, methods and applications.* J Photochem Photobiol B, 2010. **98**(1): p. 77-94.

9.	Pogue, B.W., *Optics in the Molecular Imaging Race.* Optics & Photonics News, 2015. **Sept.**: p. 25-31.

10.	Deliolanis, N., T. Lasser, D. Hyde, A. Soubret, J. Ripoll, and V. Ntziachristos, *Free-space fluorescence molecular tomography utilizing 360 degrees geometry projections.* Opt Lett, 2007. **32**(4): p. 382-4.

11.	Chen, B.C., W.R. Legant, K. Wang, L. Shao, D.E. Milkie, M.W. Davidson, C. Janetopoulos, X.S. Wu, J.A. Hammer, 3rd, Z. Liu, B.P. English, Y. Mimori-Kiyosue, D.P. Romero, A.T. Ritter, J. Lippincott-Schwartz, L. Fritz-Laylin, R.D. Mullins, D.M. Mitchell, J.N. Bembenek, A.C. Reymann, R. Bohme, S.W. Grill, J.T. Wang, G. Seydoux, U.S. Tulu, D.P. Kiehart, and E. Betzig, *Lattice light-sheet microscopy: imaging molecules to embryos at high spatiotemporal resolution.* Science, 2014. **346**(6208): p. 1257998.

12.	Herschman, H.R., D.C. MacLaren, M. Iyer, M. Namavari, K. Bobinski, L.A. Green, L. Wu, A.J. Berk, T. Toyokuni, J.R. Barrio, S.R. Cherry, M.E. Phelps, E.P. Sandgren, and S.S. Gambhir, *Seeing is believing: non-invasive, quantitative and repetitive imaging of reporter gene expression in living animals, using positron emission tomography.* J Neurosci Res, 2000. **59**(6): p. 699-705.

13.	Yang, Y., Y.C. Tai, S. Siegel, D.F. Newport, B. Bai, Q. Li, R.M. Leahy, and S.R. Cherry, *Optimization and performance evaluation of the microPET II scanner for in vivo small-animal imaging.* Phys Med Biol, 2004. **49**(12): p. 2527-45.

14.	Judenhofer, M.S. and S.R. Cherry, *Applications for preclinical PET/MRI.* Semin Nucl Med, 2013. **43**(1): p. 19-29.

15.	Lehmann, S., R. Perera, H.P. Grimm, J. Sam, S. Colombetti, T. Fauti, L. Fahrni, T. Schaller, A. Freimoser-Grundschober, J. Zielonka, S. Stoma, M. Rudin, C. Klein, P. Umana, C. Gerdes, and M. Bacac, *In Vivo Fluorescence Imaging of the Activity of CEA TCB, a Novel T-Cell Bispecific Antibody,*

Reveals Highly Specific Tumor Targeting and Fast Induction of T-Cell-Mediated Tumor Killing. Clin Cancer Res, 2016. **22**(17): p. 4417-27.

16. Tang, Q., J. Wang, A. Frank, J. Lin, Z. Li, C.W. Chen, L. Jin, T. Wu, B.D. Greenwald, H. Mashimo, and Y. Chen, *Depth-resolved imaging of colon tumor using optical coherence tomography and fluorescence laminar optical tomography.* Biomed Opt Express, 2016. **7**(12): p. 5218-5232.

17. Kepshire, D.S., S.L. Gibbs-Strauss, J.A. O'Hara, M. Hutchins, N. Mincu, F. Leblond, M. Khayat, H. Dehghani, S. Srinivasan, and B.W. Pogue, *Imaging of glioma tumor with endogenous fluorescence tomography.* J Biomed Opt, 2009. **14**(3): p. 030501.

18. Suihko, C., L.D. Swindle, S.G. Thomas, and J. Serup, *Fluorescence fibre-optic confocal microscopy of skin in vivo: microscope and fluorophores.* Skin Res Technol, 2005. **11**(4): p. 254-67.

19. Hillman, E.M., D.A. Boas, A.M. Dale, and A.K. Dunn, *Laminar optical tomography: demonstration of millimeter-scale depth-resolved imaging in turbid media.* Opt Lett, 2004. **29**(14): p. 1650-2.

20. Moon, J.A. and J. Reintjes, *Image-Resolution by Use of Multiply Scattered-Light.* Optics Letters, 1994. **19**(8): p. 521-523.

21. Zhang, R., S.C. Davis, J.L. Demers, A.K. Glaser, D.J. Gladstone, T.V. Esipova, S.A. Vinogradov, and B.W. Pogue, *Oxygen tomography by Cerenkov-excited phosphorescence during external beam irradiation.* J Biomed Opt, 2013. **18**(5): p. 50503.

22. Demers, J.L., S.C. Davis, R. Zhang, D.J. Gladstone, and B.W. Pogue, *Cerenkov excited fluorescence tomography using external beam radiation.* Opt Lett, 2013. **38**(8): p. 1364-6.

23. Dothager, R.S., R.J. Goiffon, E. Jackson, S. Harpstrite, and D. Piwnica-Worms, *Cerenkov radiation energy transfer (CRET) imaging: a novel method for optical imaging of PET isotopes in biological systems.* PLoS One, 2010. **5**(10): p. e13300.

24. Thorek, D.L., A. Ogirala, B.J. Beattie, and J. Grimm, *Quantitative imaging of disease signatures through radioactive decay signal conversion.* Nat Med, 2013. **19**(10): p. 1345-50.

25. Axelsson, J., A.K. Glaser, D.J. Gladstone, and B.W. Pogue, *Quantitative Cherenkov emission spectroscopy for tissue oxygenation assessment.* Opt Express, 2012. **20**(5): p. 5133-42.

26. Jarvis, L.A., R. Zhang, D.J. Gladstone, S. Jiang, W. Hitchcock, O.D. Friedman, A.K. Glaser, M. Jermyn, and B.W. Pogue, *Cherenkov video imaging allows for the first visualization of radiation therapy in real time.* Int J Radiat Oncol Biol Phys, 2014. **89**(3): p. 615-22.

27. Axelsson, J., S. Davis, D. Gladstone, and B. Pogue, *Cerenkov emission induced by external beam radiation stimulates molecular fluorescence.* Med Phys, 2011. **38**(7): p. 4127-4132.

28. Zhang, R., V. D'Souza A, J.R. Gunn, T.V. Esipova, S.A. Vinogradov, A.K. Glaser, L.A. Jarvis, D.J. Gladstone, and B.W. Pogue, *Cherenkov-excited luminescence scanned imaging.* Opt Lett, 2015. **40**(5): p. 827-30.

29. Keller, P.J., A.D. Schmidt, J. Wittbrodt, and E.H. Stelzer, *Reconstruction of zebrafish early embryonic development by scanned light sheet microscopy.* Science, 2008. **322**(5904): p. 1065-9.

30. Bruza, P., H. Lin, S.A. Vinogradov, L.A. Jarvis, D.J. Gladstone, and B.W. Pogue, *Light sheet luminescence imaging with Cherenkov excitation in thick scattering media.* Opt Lett, 2016. **41**(13): p. 2986-9.

31. Esipova, T.V., A. Karagodov, J. Miller, D.F. Wilson, T.M. Busch, and S.A. Vinogradov, *Two new "protected" oxyphors for biological oximetry: properties and application in tumor imaging.* Anal Chem, 2011. **83**(22): p. 8756-65.

32. Dehghani, H., M.E. Eames, P.K. Yalavarthy, S.C. Davis, S. Srinivasan, C.M. Carpenter, B.W. Pogue, and K.D. Paulsen, *Near infrared optical tomography using NIRFAST: Algorithm for numerical model and image reconstruction.* Commun Numer Methods Eng, 2008. **25**(6): p. 711-732.

33. Jermyn, M., H. Ghadyani, M.A. Mastanduno, W. Turner, S.C. Davis, H. Dehghani, and B.W. Pogue, *Fast segmentation and high-quality three-dimensional volume mesh creation from medical images for diffuse optical tomography.* J Biomed Opt, 2013. **18**(8): p. 86007.

Supplementary Data

The contrast to background ratio (CBR) was evaluated as the ratio of the mean and standard deviation intensity for the given ROI.

$$CBR = I_S/I_{sd} \qquad (1)$$

Where I_S is the mean intensity of the processed images, I_{sd} is the standard deviation intensity of the given ROI. These values were calculated and are the data graphed in Fig 5 (a)-(c).

S.2 Simulation & Reconstruction Studies

The process of CELSI tomography includes two stages: 1) generate Cerenkov radiation as 5 mm sheet-shaped LINAC beams, and 2) to use Cerenkov radiation to excite phosphors and emit luminescent light. The fluorescent photons escape the tissue, reach the body surface and are detected using a highly sensitive CCD camera. The whole process can be modeled by the coupled continuous wave (CW)-domain diffusion equations, which can be expressed as [12, 13]:

$$\nabla D_x(r)\nabla\Phi_x(r) - \mu_{ax}(r)\Phi_x(r) = -q(r) \qquad (2)$$

$$\nabla D_m(r)\nabla\Phi_m(r) - \mu_{am}(r)\Phi_m(r) = -\Phi_x(r)\eta\mu_{af}(r) \qquad (3)$$

Where Eq. (2) is the Cherenkov excitation field and Eq. (3) is the luminescence emission field. Subscripts x and m denote the excitation and emission wavelengths, respectively. $q(r)$ is the Cherenkov excitation source term at position r induced by a sheet-shaped LINAC beams, $\Phi_{x,m}(r)$ are the excitation and emission fields at position r, μ_{ax} and μ_{am} represent the absorption coefficients, $D_{x,m} = 1/\left[\left(\mu_{ax,m} + \mu'_{sx,m}\right)\right]$ is the diffusion coefficient, and reduced scattering coefficient μ'_s is equivalent to $\mu_s(1-g)$, where g is the anisotropy factor. μ_{af} is the luminescent agent absorption at the excitation wavelength, and η is the luminescence quantum efficiency. The quantity $\eta\mu_{af}$ is known as the luminescence yield. The implementation of a Robin-type boundary condition accounts for the refractive index mismatch at the tissue boundary as coded into NIRFAST [32, 33]. Note that the excitation light source in CELSI is endogenous source in tissue, which is different from the external excitation light in fluorescence imaging.

When the optical properties μ_{ax}, μ_{am}, μ'_{sx}, μ'_{sm} were assumed to be constant, the CELSI tomography reconstruction is to recover the distribution of $\eta\mu_{af}$ in tissue based on the measurements, which are defined as the emitted photons on the surface for an induced Cherenkov excitation source. The measurements can be acquired with detectors or non-contact CCD camera. Since the emission light undergoes multiple scattering events before reaching the surface, the CELSI reconstruction is a severely ill-posed problem. Therefore, the CELSI reconstruction is achieved by minimizing the difference between measured and calculated data, based on the Tikhonov regularization technique, which leads to the following updated equation :

$$\Delta\eta\mu_{af} = (J_{fl}^T J_{fl} + \lambda I)^{-1} J_{fl}^T (\Phi_{fl}^{meas} - \Phi_{fl}^{calc}) \qquad (4)$$

Where Φ_{fl}^{meas} is the measured fluorescence data, and Φ_{fl}^{calc} is the calculated fluorescence data generated by solving Eqs. (2)-(3) based on finite element method (FEM). λ is the regularization parameter, which is chosen at each iteration by scaling the maximum of the diagonal of $J_{fl}J_{fl}^T$, where J_{fl} is the Jacobian matrix calculated using the Adjoint method:

$$J_{fl} = \begin{bmatrix} \dfrac{\partial \ln I_1}{\delta\mu_{af1}} & \dfrac{\partial \ln I_1}{\delta\mu_{af2}} & \dfrac{\partial \ln I_1}{\delta\mu_{af3}} & \cdots & \dfrac{\partial \ln I_1}{\delta\mu_{afNN}} \\[2ex] \dfrac{\partial \ln I_2}{\delta\mu_{af1}} & \dfrac{\partial \ln I_2}{\delta\mu_{af2}} & \dfrac{\partial \ln I_2}{\delta\mu_{af3}} & \cdots & \dfrac{\partial \ln I_2}{\delta\mu_{afNN}} \\[2ex] \dfrac{\partial \ln I_3}{\delta\mu_{af1}} & \dfrac{\partial \ln I_3}{\delta\mu_{af2}} & \dfrac{\partial \ln I_3}{\delta\mu_{af3}} & \cdots & \dfrac{\partial \ln I_3}{\delta\mu_{afNN}} \\[2ex] \vdots & \vdots & \vdots & \cdots & \vdots \\[2ex] \dfrac{\partial \ln I_{NM}}{\delta\mu_{af1}} & \dfrac{\partial \ln I_{NM}}{\delta\mu_{af2}} & \dfrac{\partial \ln I_{NM}}{\delta\mu_{af3}} & \cdots & \dfrac{\partial \ln I_{NM}}{\delta\mu_{afNN}} \end{bmatrix} \qquad (5)$$

Where N is the number of light-sheet, and M is the number of measurements, leading to total NM measurements. NN is the number of nodes of finite element mesh. The jth column of this matrix represents the surface fluorescence due to the jth Cherenkov excitation source.

Image reconstruction was achieved using a modified NIRFAST, a finite element method (FEM)-based software package [16]. A change in projection error of less than 0.01% between iterations and the maximum iteration number were used as stopping criteria, indicating convergence.

In order to demonstrate the effectiveness of CELSI tomography, 5 sets of simulation studies were carried out, which include reconstruction results for the single source and the multiple sources, different scan modes, small inclusion with varied depths as well as resolution test. In the first two simulation results, 67 detectors were arranged on the top surface for data collections, 21 light sheet beams were used to generate Cerenkov sources. In all simulation cases, 1% noise was randomly added to the simulated data. Also, comparisons of reconstruction were performed with Epi-illumination fluorescence tomography (Epi-FT) (Fig. 5(a)) and full fluorescence tomography (Full-FT). For Epi-FT and Full-FT, the same setting as the CELSI reconstruction was used except that 21 point sources (of the excitation light field) are generated by laser beams at the surface of the measured object.

In order to generate simulated data, a 2D rectangle mesh consisting of 2747 nodes corresponding to 5280 linear triangular elements was used. The size of the phantom was 100*60 mm. The background absorption and reduced scattering properties were compiled in Table 1. The background optical absorption efficiency for the phosphor was set as $\mu_{af} = 0.002$.

Table 1. The background optical absorption and reduced scattering coefficient properties used in the simulation experiments, as well as phosphor absorption and quantum efficiency, τ.

Wavelength band	μ_{ax} [mm^{-1}]	μ'_{sx} [mm^{-1}]	μ_{af} [mm^{-1}]	τ
Excitation	0.009	1.314	--	--
Emission	0.006	1.273	0.002	0.1

In the first case, a single fluorophore inclusion with a radius of 5 mm was placed at the center of the mesh. The inclusion was assumed to have the same background absorption coefficients, and reduced scattering coefficients but with 4 times of fluorophore absorption coefficient. In the CELSI reconstruction, the initial guesses of the inclusion were assumed to be background optical properties. An initial regularization parameter of $\lambda = 0.01$ and a reconstruction pixel basis of 30×30 (x and y spatial discretization) uniform cells were used. The corresponding results are shown in Fig. 5. The numerical results reveal a clear improvement of the distribution of reconstructed fluorophore for CELSI tomographic reconstruction.

S.3 Reconstruction Matrix Conditioning

The effects on reconstructed images for different scan modes of light sheet were also considered. Here, reconstructed results for scan modes of horizontal, vertical, and angles of 45 degree were reported, as shown in Fig. 5. We use two approaches for comparing the performance of different scan patterns. In order to demonstrate the idea that CELST data will provide quantifiable improvements compared to the FT techniques (Epi/Full-FT), SVD matrics were used to examine the matrix formed by the discretization of the forward problem. The singular value curves for the FT and CELST imaging schemes for the given geometry were plotted in Fig. S.1. The curves show that the CELST yields smaller singular value decay and has better favorable conditioning than FT. The curves also demonstrate that the summed scan mode results in significant corresponding increases in the number of singular values above a given threshold, which corresponds to a larger number of image-space modes available for reconstruction, which is aligned with the Fig. S.1 The other approach is to look at the rank of the Jacobian, which indicates the number of independent measurements. From the Fig. S.1(c) it clearly shows that the summed scan mode has larger number of independent measurements.
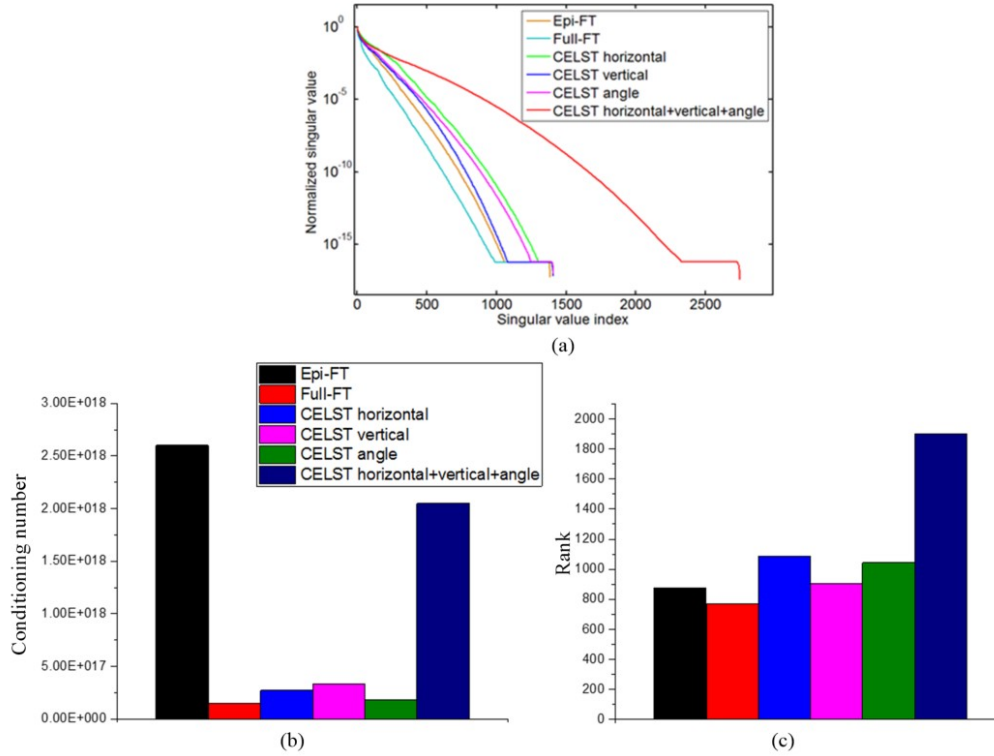

Figure S.1 The singular value curves (a) for the FMT and CELSI techniques are shown. In (b) the conditioning number and (c) the rank of Jacobian are shown for different scan modes.